Efficient photocatalytic degradation of crystal violet dye and electrochemical performance of modified MWCNTs/Cd-ZnO nanoparticles with quantum chemical calculations

M.F. Sanakousar[a], Vidyasagar. C.C[a,*], Victor M. Jiménez-Pérez[b], B.K. Jayanna[c], Mounesh[d], A.H. Shridhar[e], K. Prakash[f]

[a] Department of Studies and Research in Chemistry, Rani Channamma University, Belagavi 591156 Karnataka, India
[b] Universidad Autónoma de Nuevo León, Facultad de Ciencias Químicas, Ciudad Universitaria, Av.Universidad s/n. C. P. 66451, Nuevo León, Mexico
[c] Department of Chemistry, BNMIT, Bengaluru 560070, Karnataka, India
[d] Department of Studies and Research in Chemistry, Vijayanagara Srikrishnadevaraya University, Ballari 583105 Karnataka, India
[e] Department of Chemistry, SVM Arts Science & Commerce College, Ilkal, Karnataka, India
[f] Department of Environmental Science, Gulbarga University, Kalaburagi 585106, India

ARTICLE INFO

ABSTRACT

Several literature studies have defined the doping technique of ZnO with a Cd (transition metal) for photocatalysis applications. Despite this, the properties and the mechanism behind it have never been completely explained. The present work outlines the effect of Cadmium ion doping on structural, optical, electrochemical impedance and photocatalytic properties of ZnO and Cd-ZnO nanoparticles prepared via simple precipitation method. The prepared Cd-ZnO was characterized using advanced techniques such as powder X-ray diffraction, field-emission scanning electron microscope fitted with energy dispersive X-ray diffraction, UV-visible absorbance spectroscopy and electrochemical impedance were performed on modification of glassy carbon electrode (GCE) with multi-walled carbon nanotubes decorated with ZnO and Cd-ZnO. Moreover, Cd-ZnO NPs displayed superior electrochemical performance than undoped ZnO NPs. Experiments revealed that, as compared to ZnO and higher dopant concentration, the photodegradation of crystal violet was enhanced by the use of 0.5 mol% Cd-ZnO catalyst. The implantation of Cd is assisted by faster carrier separation and transfer efficiency. Tauc's plots illustrate that the incorporation of Cd ion has decreased the optical band-gap of ZnO samples. After Cd doping, the valence and conduction band of ZnO were modified, contributing to the development of O_2^-, resulting in a significant improvement in photodegradation. Mulliken atomic charges and molecular properties computed at B3LYP/6-31G level of theory. The HOMO-LUMO band gap of alleged photocatalysts was calculated using density function theory (DFT). Further to support our hypothesis on degradation of the dye using Cd-ZnO was confirmed by the IR and Mass spectral studies. Computational prediction of toxicity of degraded organic molecules was estimated by Toxicity Estimation Software Tool (TEST) by United States Environmental Protection Agency. FTIR and Mass spectroscopy confirm the 100% degradation of CV-dye under UV chamber (6 W) after 30 min at basic medium. The enhanced electrochemical and photocatalytic efficiency of Cd doped ZnO nanoparticles suggest that they have dual activity in energy and water treatment applications.

1. Introduction

As the global textile dyeing industry expands, more fresh water resources are contaminated, with harmful compounds entering rivers, ponds, and lakes through numerous pathways, endangering the natural environment's harmonious growth (Aqeel et al., 2020). Because polluted water is usually present in large amounts and contains deep coloring agents with significant toxicity, if we do not clean it appropriately be-

fore releasing it into water resources, it may cause serious health effects to humans. To maintain a continuous supply of these critical nutrients to all kinds of life, dye-containing waste water must be treated (Yuan et al., 2019; Spitaleri et al., 2019; Mittal et al., 2014). According to reports, 15% of synthetic industrial wastes, particularly textile and pharmaceutical wastes, are unintentionally mixed with the main water streams (Jayaraman et al., 2020). Because the contaminated matrix in the water stream gradually reduces sunlight penetration, disrupting the biological

---

M.F. Sanakousar, Vidyasagar. C.C, Victor M. Jiménez-Pérez et al.

Journal of Hazardous Materials Advances 2 (2021) 100004

process in the aquatic environment, so environmental protection has become a high priority (Zhu et al., 2009). Because of the inertness of dye molecules in waste water to light, heat, and oxidative agents, decolorization becomes a major challenge (Ghosh et al., 2015). Chemical, physical, and biological treatment approaches for polluted dye water have all proved effective in the past. Various removal methods such as liquid membrane separation (Dâas and Hamdaoui, 2010), biological treatments (El-Naas et al., 2009; Zhang et al., 2011), oxidation (Gomes et al., 2008), electrolysis (Xie et al., 2019), adsorption (Chen et al., 2020), chemical catalytic degradation (Chimupala et al., 2020) and few commonly used methods such as ultra-filtration, desalination and reverse osmosis (Yuan et al., 2019; Spitaleri et al., 2019; Mittal et al., 2014). Various removal strategies, such as liquid membrane separation, are now being researched in a number of studies. However, the effectiveness of degradation, environmental implications, and costs of various chemical and physical techniques vary. These procedures can sometimes eliminate dangerous pollutants, but they can also result in the production of unwanted substances and health concerns (Zhang et al., 2019). Photocatalysis is a much more comparable and efficient approach than all the others. When light is allowed to fall on the catalysts, they quickly decolorize the dyes, especially textile dyes, utilizing sunlight as the energy source and oxygen from the atmosphere as the oxidant, hazardous compounds are broken down into non-toxic compounds. During the photocatalytic process, an efficient photocatalyst may operate as an effective material, and researchers have always found it difficult to develop the desired shape, size, and porosity while keeping costs low (Wang et al., 2013; Kong et al., 2019; Sakib et al., 2019). The researchers are employing visible light sensitive band gap materials for more efficient photocatalytic degradation. Titanium dioxide (TiO_2) (Xie et al., 2019), Zinc oxide (ZnO) (Venkatesha et al., 2012), Copper oxide (CuO) (Sakib et al., 2019), Ferric oxide (Fe_2O_3) (Boruah et al., 2017), Zinc sulphide (ZnS) (Soltani et al., 2012) and Cadmium Sulphide (CdS) (Soltani et al., 2012) belong to a class of photocatalysts, amongst them at ambient temperature, ZnO is an n-type semiconductor with a high band gap of 3.36 eV that processes excitonic optically driven ultraviolet (390 nm) lasing action. ZnO has high radiation hardness, thermal properties, effective transparency, structural stability, biological compatibility, and efficient UV-range optical absorption (Pirsaheb et al., 2020). As a result, ZnO has the wide range of potential applications, including solar cells, optoelectronics, antimicrobial goods, and photocatalysis. ZnO responds to just 5% of UV energy in the sun spectrum and 0.1 percent of UV radiation in indoor illumination because of its good biocompatibility, strong redox properties (Neelgund and Oki, 2019; Kiriarachchi et al., 2019; Shafi et al., 2019; Lavand and Malghe, 2015) and large band gap. Incorporation of transition metal ions is an efficient tool to tailor the desired properties in order to utilize the maximum sunlight, and slight changes in physical and chemical properties at nano levels (Vidyasagar et al., 2011). Herein, we have reported the rapid photocatalytic degradation of CV using Cd-ZnO nanoparticles. Despite the fact that several researchers have developed Cd-ZnO catalyst, but the photocatalytic degradation of CV has not been thoroughly studied. The implementation of Cd ions into ZnO cause defects and improve visible harvesting ability of ZnO. The IR and mass spectral experiments confirmed our hypothesis on dye degradation, the spectral results are considered to be in close agreement with theoretical values.

2. Experimental section

2.1. Materials

The organic dyes Crystal violet (CAS number: 548-62-9), Alizarin Red S (ARS) (S. D. Fine-Chem. Ltd., India), Zinc acetate [Zn ($CH_3COO)_2$. H_2O] (98.7 %, HiMedia), cadmium chloride monohydrate [$CdCl_2$. H_2O] (99.1 % HiMedia), Sodium hydroxide [NaOH] (98 % HiMedia) and ethanol [C_2H_5OH] (99.9 %, S. D. Fine-Chem. Ltd.) were procured and used without further purification. All of the compounds employed in

this work were of analytical grade, and the research was carried using deionised water was used throughout the study. The organic dyes Crystal violet (CV) & Alizarin Red S (ARS) were used without further purification (S. D. Fine-Chem. Ltd., India).

2.2. Preparation of ZnO and Cd-ZnO nanoparticles

In the present work, ZnO and Cd-ZnO [0.5, 1.0, 1.5 and 2.0 at mol% of Cd] nanoparticles were synthesized via PVA assisted chemical method. 1.0 g of zinc acetate was taken in 100 ml ethanol and kept for constant stirring for 24 h. 25 ml double distilled water was added drop wise (9-10/min) and pH was recorded at 6.01. Then 0.4 N NaOH was added drop wise (8-10/min) to obtain pH 10 under slow stirring for 24 h. The resultant precipitate was washed in an ultrasonic bath twice with deionised water and ethyl alcohol. Finally, the powder was dehydrated in an oven at 60 °C and subsequently annealed at 500 °C (8 °C/min) for 2 h. The similar protocol has been followed for the preparation of Cd-ZnO samples [0.5, 1.0, 1.5 and 2.0 at mol% of Cd] with the addition of cadmium chloride monohydrate ($CdCl_2$. H_2O) solution drop wise (9-10/min) to the mixture of zinc acetate ($ZnC_4H_6O_4$) and ethyl alcohol.

2.3. Characterization of powder samples

Powder X-ray diffractometer (BRUKER: D8 advance) connected with Cu-Kα radiation at = 0.154 nm in the range of 2θ values 10°-80° was recorded to analyze the crystalline nature of prepared ZnO and Cd-ZnO nanoparticles. The size distribution and surface morphology of the nanoparticles were captured using Carl Zeiss AG-ULTRA 55 field emission scanning electron microscope (FE-SEM) equipped with an energy dispersive X-ray spectroscopy (EDAX). A UV-Visible spectrophotometer was recorded to quantify the optical absorbance using model USB 4000, Ocean Optics, USA. Using KBr pellets, IR spectra were recorded using a Perkin Elmer spectrum RX-1model spectrophotometer. Shimadzu LCMS 2010A software and the ESI ionization technique were used to obtain mass spectra.

2.4. GCE surface modification technique

The GCE (0.070 cm^2) was carefully polished with 0.3 mmol and 0.05 mmol alumina, followed by successive sonication with 1:1 deionised water and ethanol for 3 minutes to achieve a mirror-like surface. Then, 0.5 mmol of a ZnO and 0.5 mol% MWCNTs (Multi-walled carbon nanotubes) hybrid suspension was dropped on the clean surface of a glassy carbon electrode (GCE), which was prepared by dispersing ZnO and MWCNTs in a dry DMF/Nafion mixture with the aid of ultrasonic treatments followed by drying under an infrared light. Similar technique has been followed to prepare 0.5 mol% Cd-ZnO/GCE and Cd-ZnO/GCE/MWCNTs electrode for comparison.

2.5. Photochemical measurements

Without further purification, the organic dyes (CV and Alizarin Red S) were procured from S. D. Fine-Chem. Ltd., India) were used. Throughout the study, deionised water was employed. A 6W UV-A lamp was used in a constructed reactor (Philips, India). At 365 nm, the maximum emission intensity was achieved. The dye solution and catalyst mixture were irradiated perpendicular to the solution at room temperature. Between the source and the solution, a 16-cm gap was maintained. To analyze photo degradation, a 50 mL dye solution with appropriate concentrations of CV (10 mg/L) and ARS (10 mg/L) was placed in a 100 mL beaker. The effect of pH on dye photo degradation was studied over a pH range of 2.0 to 12.0, and the pH of the solution was changed using NaOH/H_2SO_4 solutions and a pH meter (Equiptronics, Elico-LI 120). Experiments were also carried out with catalyst doses ranging from 0.5
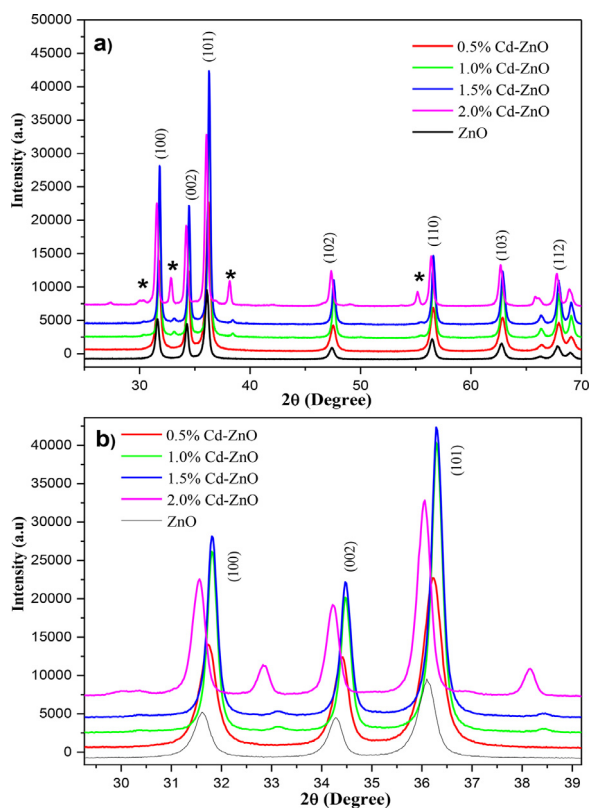
Fig. 1. (a) X-ray diffraction pattern of bare ZnO and Cd-ZnO ($0.0 \leq X \leq 2.0$ mol%) crystals calcinated at 500 °C and (b) Insight view of shifting peak positions of ZnO and Cd doped ZnO (1 0 0), (0 0 2) and (1 0 1) planes.

mg to 3.0 mg/50 ml. A double beam UV-1800 ultraviolet–visible spectrophotometer was used to measure absorbance in 1 cm quartz cuvettes (Shimadzu, Japan).
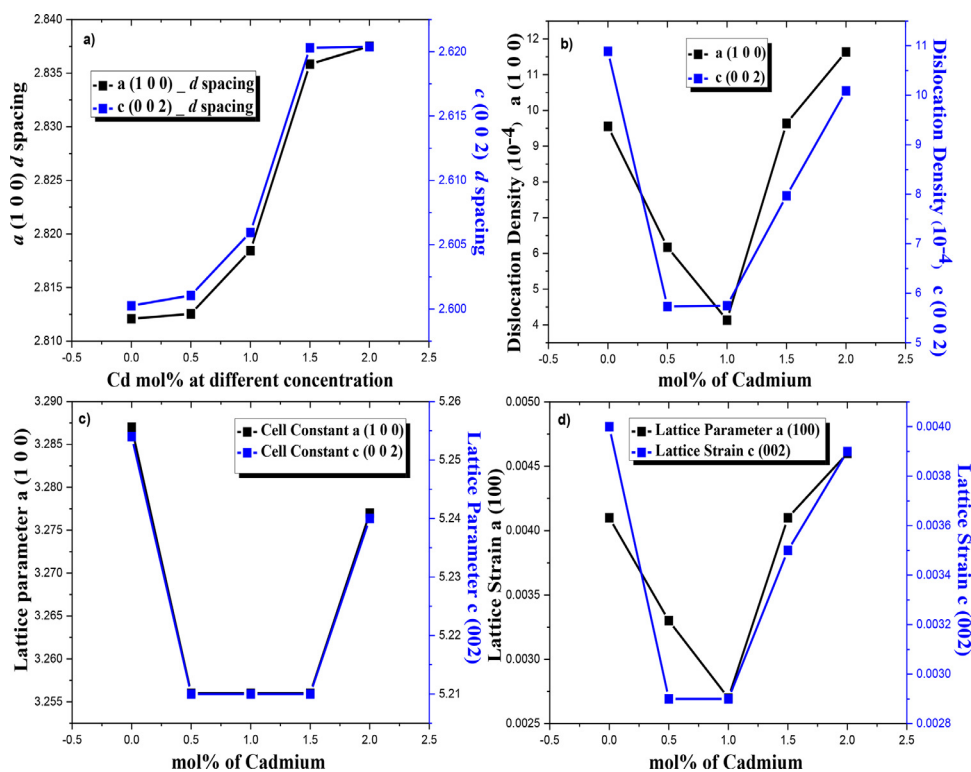
2.6. In silico eco-toxicity prediction

Because transitional compounds are produced during photocatalytic degradation, it is critical to know their chemical structure and forecast their toxicity. In the recent past, several research have progressively used in silico based toxicity tools/programs that are based on computer simulation (Williams et al., 2017; Singh et al., 2021). Toxicity Estimation Software Tool (TEST) is a computer program that estimates the toxicity of chemical compounds using one of the several advanced Quantitative Structure Activity Relationships (QSARs) technologies developed by the US Environmental Protection Agency. It takes user input in the form of a chemical structure drawing window or a simple SMILES text file. Without the use of additional programs, such as chemical descriptors, the data is processed for toxicity prediction (Martin et al., 2012). The CompTox Compounds Dashboard is a single-window knowledge-base with 875,000 chemicals that can be searched for toxicity and exposure information. To limit the need of animal models for chemical study, the EPA has combined use, physicochemical attributes, exposure, environmental fate and transport, in vitro bioassay, and in vivo toxicity. Chemical identities, classifications, and genes/assays related to high-throughput data may all be used to search it. The fish (*Fathead minnow*) (LC50) 96-hr, water flea (*D. magna*) (LC50) 48-hr lethal concentration (50 %), and Hymenostome (*T. pyriformis*) (IGC50) 48-hr Inhibition Growth Concentration (50 %) tests were all specifically predicted because the results of these tests are the most widely used methods to predict ecotoxicological endpoints.

3. Results and discussion

3.1. Structural characteristics (PXRD)

Fig. 1 shows the powder x-ray diffractograms of undoped and Cd-ZnO samples at different concentrations peak positions (2θ) and relative peak intensities are consistent with the JCPDS card No.: 79-0208 (a = 0.3264 nm and c = 0.5219 nm). The figures illustrate the phase purity of ZnO and Cd-ZnO (Cd = 0.0 to 2.0 %) and shows a typical

Fig. 2. The change in the *d* spacing (a), Dislocation density (b), Lattice parameter (c) and Lattice strain (d) of ZnO with different cadmium concentration.

M.F. Sanakousar, Vidyasagar. C.C, Victor M. Jiménez-Pérez et al.

Journal of Hazardous Materials Advances 2 (2021) 100004

Table 1

Data on 2θ, peak intensity, FWHM, d-spacing and relative intensity in %.

mol % Cd doping	(hkl)	Pos. [°2Th.]	Height [cts]	FWHM [°2Th.]	d-spacing [Å]	Rel. Int. [%]
ZnO	(1 0 0)	31.7957	16754.26	0.2668	2.8121	55.89
	(0 0 2)	34.4639	26630.43	0.2868	2.60025	88.83
0.5 mol% Cd-ZnO	(1 0 0)	31.7905	22816.66	0.2145	2.81255	63.08
	(0 0 2)	34.4527	16872.4	0.2081	2.60106	46.64
1.0 mol% Cd-ZnO	(1 0 0)	31.7222	20377.63	0.1755	2.81845	62.45
	(0 0 2)	34.386	14789.85	0.2083	2.60596	45.33
1.5 mol% Cd-ZnO	(1 0 0)	31.5226	15175.7	0.2678	2.83584	60.66
	(0 0 2)	34.192	11289.73	0.2452	2.6203	45.13
2.0 mol% Cd-ZnO	(1 0 0)	31.5036	12185.99	0.2944	2.83751	61.45
	(0 0 2)	34.1909	9710	0.2759	2.62038	48.96

Table 2

Data on Lattice constants, lattice strain, unit cell volume, Bond length and c/a ratio of bare ZnO and Cd-ZnO nanoparticles by Debye-Scherrer Method.

SampleAt different Cd mol%	Lattice Constants (Å)		Debye-Scherrer Method							Unit Cell Volume (Å)³	Bond Length (Å)	c/a ratio
			Lattice Strain (ε) x10⁻³		Dislocation density (δ) x10⁻³		Crystal Size (nm)					
	a (100)	c (002)	a (100)	c (002)	a (100)	c (002)	a (100)	c (002)				
ZnO	3.2471	5.2005	1.12	1.196	0.956	1.089	32.35	30.30		47.48	5.559	1.601
0.5 mol% Cd	3.2475	5.2021	0.9	0.868	0.618	0.573	40.24	41.76		47.51	5.561	1.601
1.0 mol% Cd	3.2544	5.2119	0.737	0.869	0.414	0.575	49.17	41.71		47.80	5.572	1.601
1.5 mol% Cd	3.2745	5.2406	1.125	1.17	0.964	0.797	32.21	35.42		48.66	5.602	1.601
2.0 mol% Cd	3.2764	5.2407	1.237	1.151	1.165	1.009	29.3	31.48		48.71	5.603	1.601

diffraction intense peaks at 2θ = 31.62°, 34.28°, 36.12°, 47.39°, 56.45°, 62.71° and 67.77°, which corresponds to (1 0 0), (0 0 2), (1 0 1), (1 0 2), (1 1 0), (1 0 3) and (1 1 2) Bragg's reflection planes of wurtzite hexagonal crystal structure and additional impurity peaks correspond to ZnO_2 and $Zn(OH)_2$ were not detected. Two additional peaks of (1 1 1) at 32.82° and (2 0 0) at 38.16° belonging to cubic phase were found for 2.0 mol% Cd dopant as star marked in the (Fig. 1 and 2), which indicates the presence of a new phase or nucleating centres or segregation of Cd ions within the ZnO lattice (Joishy et al., 2018). The variation of major (1 0 0), (0 0 2), and (1 0 1) planes as a function of incorporation was observed to verify the appropriate distributions of Cd^{2+} ions in the ZnO lattice. Cadmium ions incorporation affects the d-spacing, lattice parameters, and unit volume of Cd-ZnO, as observed by the difference in diffraction angles. The XRD data was used to calculate the lattice parameters for ZnO and Cd-ZnO crystals (Table 1). A 3.2471 Å and 5.2005 Å were found to be the lattice constants a and c for ZnO, respectively. In the case of Cd-ZnO, the lattice constant a increases to 3.2475 Å and c increases to 5.2021 Å, indicating that increasing Cd doping enhances lattice constants (Table 2). Because the Cd^{2+} ion has a greater ionic radius (0.97 Å) than the Zn^{2+} ion (0.74 Å), Cd^{2+} ions are doped homogeneously in substitution mode only into the ZnO lattice and causes a modify in the lattice constants following Cd doping. The peak intensity of (1 0 0), (0 0 2), and (1 0 1) increased as the full width at half maximum (FWHM) decreased at 0.5 and 1.0 mol percent Cd^{2+} doping, indicating a possible change in crystal size. Additional Cd peaks were absent due to the high solubility of Cd^{2+} in ZnO (Tables 2 and 3). However, the relative peak height and FWHM of the ZnO doped at 1.5 and 2.0 mol% are slightly decreased compare to the sample doped at 0.5 mol%, indicating deterioration in crystal size and quality. As the Cd doping (0.5 to 1.5 %) increases, all the diffraction peak positions faintly shifted towards higher diffraction angle indicating the distortion of particularly a-axis (1 0 0) and contraction in the Cd-ZnO lattice due to pressure stress. However, at higher Cd^{2+} doping percentage (2.0 mol%), all the XRD peaks shifted towards a low diffraction angle indicate the Cd-ZnO lattice expansion due to tensile stress (Jiang et al., 2016). This attributed evidently that the Cd doping deformed a-axis of ZnO crystals. Further we have calculated the lattice strain, dislocation density, crys-

tal size, unit cell volume, bond length and c/a ratio for undoped and Cd doped ZnO samples from Debye-Scherrer Method and William-Hall Method, the percentage dependence of Cd with lattice parameter a and c for undoped and Cd doped ZnO crystals (Figs. 2 and 3) and tabulated in Tables 2 and 3. However, the William-Hall method yields crystallite sizes consistently smaller than those obtained from Scherrer's method. The small divergence in the crystallite size due to using most intense peak in the Scherrer's equation, whereas William-Hall approach an average value of several peaks, but calculations are found to be closely matched (Fig. 4). This proved that micro-strain is inversely proportional to crystalline size (Tables 2 and 3). By inspecting all the graphs, it is clear that with increasing Cd dopant the crystalline quality of the samples have been changed, which may be affected by the saturation of new nucleating centres at ZnO lattice.

Bragg's law was used to calculate the lattice parameters for hexagonal wurtzite ZnO and Cd-ZnO crystals ($2dsin\theta = n\lambda$): (Yathisha et al., 2016)

$$\frac{1}{d^2} = \frac{4}{3}\left\{\left(\frac{h^2 + hk + k^2}{a^2}\right)\right\} + \left(\frac{l^2}{c^2}\right)$$

The average crystalline size was calculated from the Scherrer's equation

$$(D) = \frac{0.9\lambda}{\beta \cos\theta}$$

where λ=wavelength (Cu-Kα 1.5406 Å), θ= Bragg's diffraction angle and β= Full width at half maxima in radians along (1 0 0) and (0 0 2) planes.

Unit volume (V) = 0.866 x a^2 x c where a is the lattice constants and V is the unit volume in (Å³)

Bond length of ZnO is given by

Bond length (L) = $\sqrt{\frac{a^2}{3} + (\frac{1}{2} - u^2) + c^2}$ (Vidyasagar et al., 2018)

where $u = \frac{a^2}{3c^2} + 0.25$ is the hexagonal structure of ZnO's potential parameter.

Micro strain (ε) = $\beta cos\theta / 4$

M.F. Sanakousar, Vidyasagar. C.C, Victor M. Jiménez-Pérez et al.

Journal of Hazardous Materials Advances 2 (2021) 100004

Table 3

Data on lattice strain, dislocation density and crystal size bare ZnO and Cd-ZnO nanoparticles by William-Hall Method.

| Sample At different Cd mol % | William-Hall Method | | | | | | Band gap (eV) |
| | Lattice Strain (ε) x10^{-3} | | Dislocation density (δ) x10^{-5} | | | Crystal Size (nm) | |
	a (100)	c (002)	a (100)	c (002)	a (100)	c (002)	
ZnO	1.12	1.196	1.0424	1.188	30.97259	29.01298	3.11
0.5 mol% Cd	0.900492	0.86761	0.6738	0.6255	38.52392	39.98399	2.75
1.0 mol% Cd	0.736891	0.8686	0.4512	0.6692	47.07681	39.9384	2.60
1.5 mol% Cd	1.124997	1.023005	1.0516	8.6963	30.83609	33.91038	2.78
2.0 mol% Cd	1.236798	1.151093	1.2710	1.1010	28.04864	30.13701	2.75
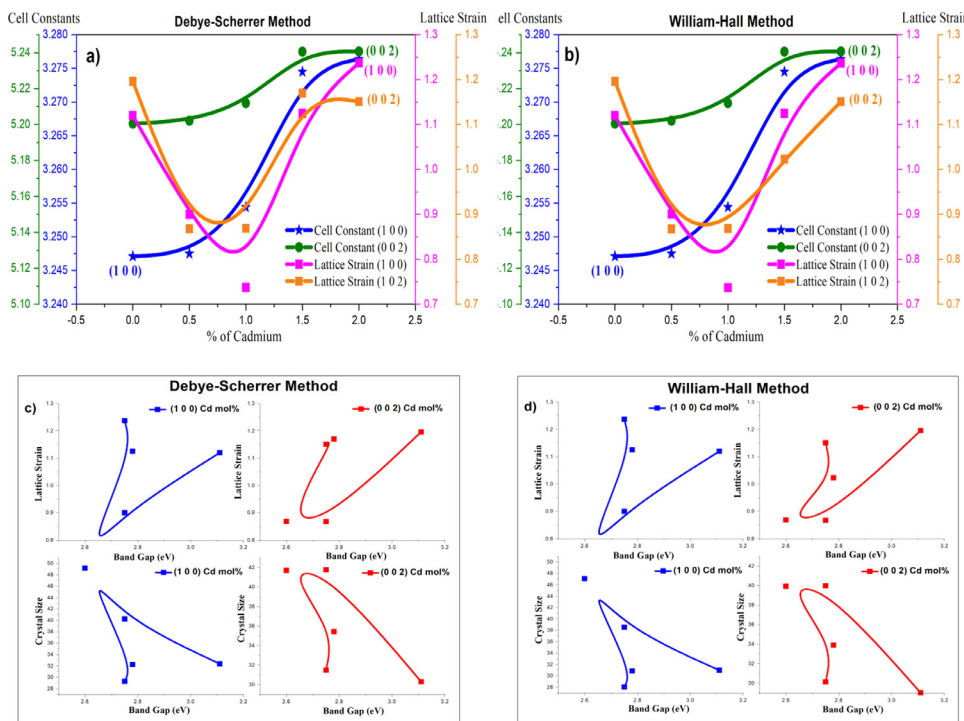
Fig. 3. Comparison of Debye-Scherrer Method and Willium-Hall Method for the cell constants, Lattice strain (a) and Crystal size, Band gap of ZnO with different Cd concentration.

Dislocation density (δ) = 1/D^2

Using the William–Hall equation, the lattice strain and crystalline size of each sample were calculated:

$$\beta \cos\theta = \frac{0.9\lambda}{D_{WH}} + 4\varepsilon \sin\theta$$

where D_{WH} is the average crystalline size, θ is Bragg's diffraction angle and ε is the strain and β is the FWHM (in radians). The plot of cos vs 4sin (Fig. 4) in the William-Hall method provides a straight line with the intercept ($\frac{0.9\lambda}{D_{WH}}$) equal to crystalline size and slope (ε) equal to micro-strain.

3.2. SEM and EDAX analysis

The absence of close packed morphology in the FESEM micrograph of pure ZnO displays the polycrystalline structure (Fig. 5).

The configuration of various sub-micrometer crystallites shows agglomeration in specific locations of the Cd-ZnO powder is also obvious in the images. There is a variation in surface morphology among Cd-ZnO particles and pure ZnO. Pure ZnO and Cd-ZnO semiconducting nanoparticles were originated to have crystallite sizes of around 31 and 67 nm, respectively. Due to agglomeration, determining the exact grain size from FESEM images is more difficult than determining the sizes using XRD data. The EDAX spectrum of ZnO is indicating the purity of the samples (Fig. 5c) and the presence of Zinc, Oxygen and Cadmium were observed in Cd-ZnO (Fig. 5d).

3.3. UV-visible spectral analysis

At room temperature, the UV-Visible spectra in the wavelength range 280-800 nm as a function of Cd concentration were recorded (Fig. 6). In comparison to bare ZnO, the optical absorption edge of Cd-ZnO (0.5 mol%) has been shifted distantly towards longer wavelength region (Fig. 6). ZnO has an optical absorption range of 340-400 nm, whereas Cd-ZnO samples have a broad absorption range of 340-400 nm in the UV region with extended shoulder peak in the visible region of 450-500 nm. The absorption edge has a large red shift when Cd doping increases (0.5 to 1.5 mol%). This reveals the major light absorption at visible region and also exhibits low absorbance in the UV region with decreasing band gap for the Cd doped samples (Cd = 0.5 - 1.5 mol %) (Chithambararaj et al., 2013). This attribution of optical absorption depends on several factors: a) secondary electronic state formation through Cd^{2+} and transition of electrons between partially forbidden bands, b) may be delocalized s- or p-type related electrons of Zn and O interact via spin exchange and c) after incorporation, the energy distribution of the allowed states changes. It was also found that the calculated band gap of 2.0 mol% Cd-ZnO increases, which may be attributed to the Burstein-Moss phenomenon caused by an increase in carrier concentration (Vidyasagar et al., 2011). Fermi level moves into the conduction band when carrier concentration is increased by 2.0 mol% Cd-ZnO. In dopants, electrons may jump to energy levels above the Fermi level of the conduction band, where optical gap will be corresponding to E (ac-
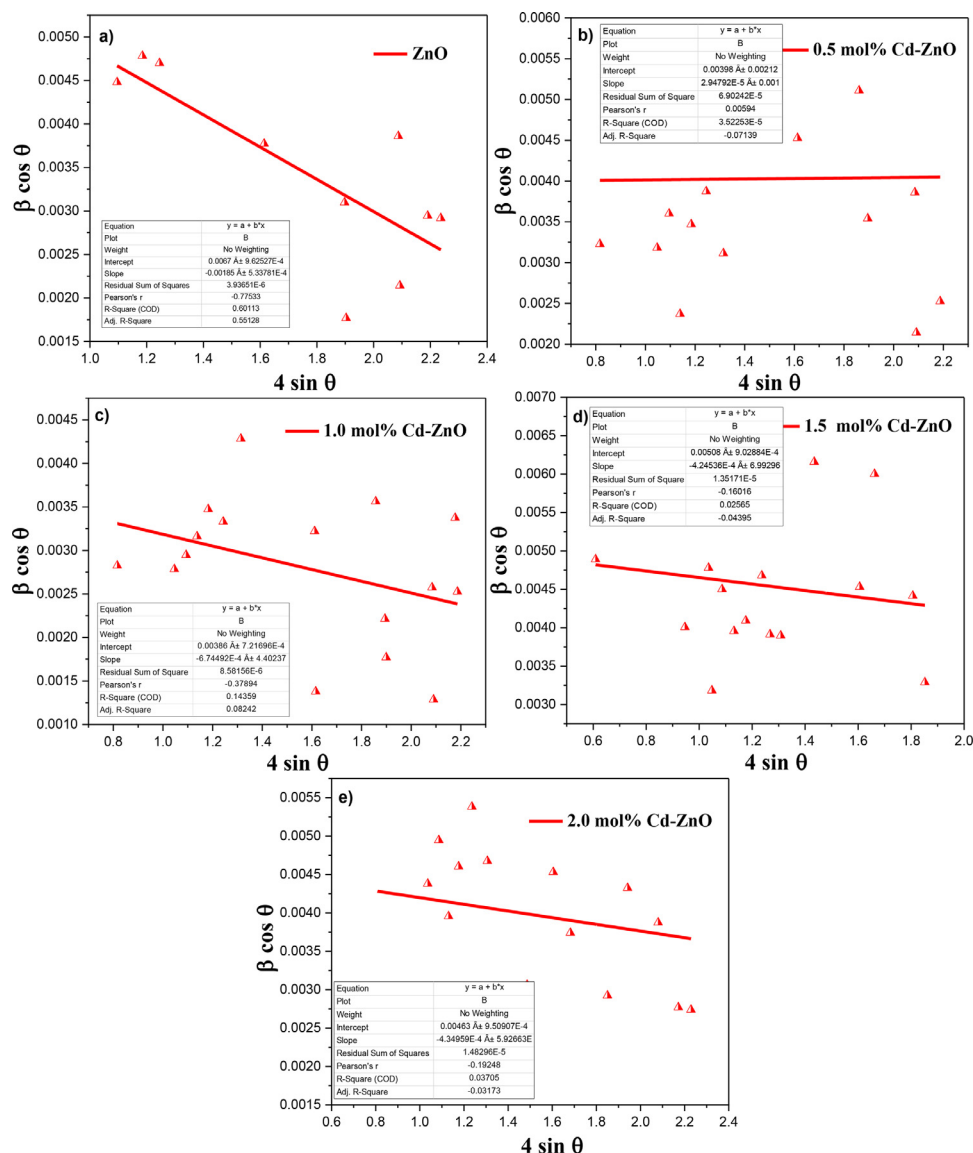
M.F. Sanakousar, Vidyasagar. C.C, Victor M. Jiménez-Pérez et al.

Journal of Hazardous Materials Advances 2 (2021) 100004

Fig. 4. The Willium-Hall analysis of bare ZnO and Cd-ZnO crystals. Fit to the data, the strain and crystal sizes are extracted from the slop and y-intercept of the fit, respectively.

tual E_g) + dE (Moss-Burstein effect) (Obeid et al., 2019). The energy band gap was calculated using $(\alpha h\nu)^{1/n}$ =A(hν-E_g), Where h is Plank's constant (6.626×10^{-34} J s), A is an energy-independent constant, α is the absorption coefficient, n is the optical transition of semiconductor and E_g is the optical band (eV). The absorption coefficient was determined with the following formula: $\alpha = 2.3030(A)/t$, where t thickness of the sample (Obeid et al., 2019). The band gap (E_g) (eV) for all the samples was calculated by projecting the linear component of the shoulder curves to the x-axis, as shown in Tauc's plots (Fig. 7). The optical band gap values determined for as prepared ZnO, 0.5, 1.0, 1.5, and 2 mol% Cd-ZnO are 3.11, 2.75, 2.60, 2.78, and 2.75 eV, respectively (Table 3). During thermal breakdown process, the band gap of ZnO lowers up to 1.0 mol% of Cd doping compare to defects free ZnO. The band gap of ZnO, on the other hand, rises from 1.5 to 2.0 mol% of Cd doping due to the Moss-Burstein effect, as observed by Mazhdi et al (Mazhdi and Tafreshi, 2020).

3.4. Electrochemical impedance studies

Electrochemical impedance spectroscopy (EIS) measurements were used to investigate electrochemical characteristics. EIS has also been used to characterize the modified electrodes' interface properties (Figs. 8

and 9). At higher frequencies, the half circle section corresponds to partial charge-transfer process and charge-transfer resistance is represented by the semicircle diameter (Rct). The Rct value for ZnO/GCE was around 76.80 Ω, which was substantially higher than the Rct value for bare GCE (46.7 Ω) (Fig. 8a), suggesting that the redox probe's electron-transfer kinetics were inhibited at the electrode interface. When compared to the ZnO/GCE (Fig. 8b) modified electrode, the Rct value was dramatically reduced from 76.80 to 26.6 Ω, implying a significantly lower the charge-transfer resistance at the ZnO/MWCNTs/GC modified electrode (Fig. 8c). The electrode's charge-transfer resistance (R_{et}) is a significant characteristic, where semicircle diameter of EIS is commonly known to be equivalent to R_{et} in the Nyquist diagram. The EIS of several electrodes is seen in (Fig. 9). The high-frequency region of the 0.5 mol% Cd-ZnO/MWCNTs/GC electrode exhibits a very small semicircle (curve c = 4.26 Ω). R_{et} increased after loading the 0.5 mol% Cd-ZnO/GC electrode probe compared to the 0.5 mol% Cd-ZnO/MWCNTs/GC electrode (curve b = 13.8 Ω). It's conceivable that the 0.5 mol% Cd-ZnO/GCE probe created a barrier that hindered electron transmission. Because the captured 0.5 mol% Cd-ZnO/GC electrode with its non-electroactive characteristics obstructs electron transport, the semicircle increased significantly (curve a = 10.6 Ω) when the semicircle was blocked by a bare GC electrode (curve a = 10.6 Ω). R_{et} increased much more after subse-
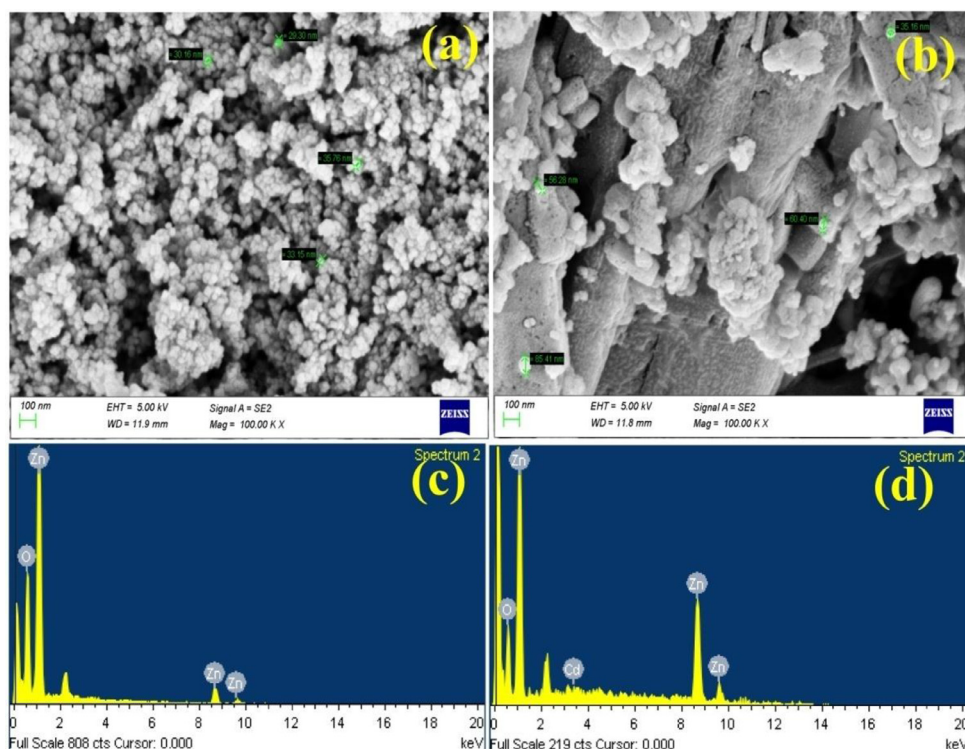
Fig. 5. FESEM images of (a) pure ZnO nanoparticles, (b) 0.5 mol% Cd-doped ZnO nanoparticles and EDAX spectrum of (c) Pure ZnO and (d) 0.5 mol% Cd-doped ZnO.
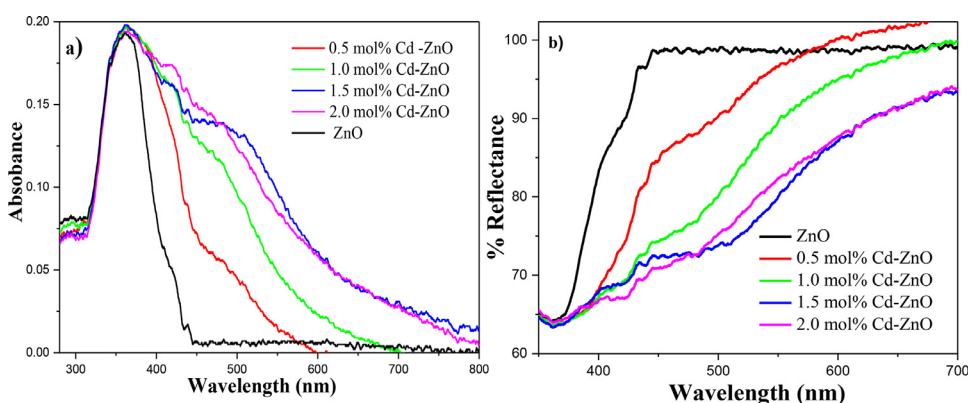

Fig. 6. (a) UV-Visible absorption spectra of bare ZnO and Cd-ZnO (0.0 ≤ X ≤ 2.0 mol%) crystals calcinated at 500 °C and (b) reflectance of the same samples.

quent deposition onto the bare GC electrode surface (curve a), indicating that the 0.5 mol% Cd-ZnO/MWCNTs/GC electrode restricted electron transfer.

3.5. Quantum chemical calculations

Using the Gaussian 09 program, the B3LYP/6-31G density functional theory method with 6-31G (d,p) basis set is applied to refine the geometrical structure of Cd-ZnO (Chandraboss et al., 2014; Aljawfi et al., 2020). The excitation energy was computed using TD-DFT, and the HOMO/LUMO energies were studied using optimized structures at the B3LYP/6-31G stage (Banu and Dheivamalar, 2020; Hadipour et al., 2015). Furthermore, chemical parameters, dipole moment (8.6601D), polarizability, band gap (E_g = 2.3560 eV), electron affinity (A = 3.3650 eV), global hardness ($\acute{\eta}$ = 1.1780), global softness (S= 0.5890), electro negativity (χ = 4.5430), chemical potential (μ = -4.5430), electrophilicity index (ω = 8.7601), ionization potential (I =5.7210 eV) and Mulliken charge distribution of each atom (Cd = 0.238234, Zn = 0.230170 and O = -0.468403) in the different sites of Cd-ZnO (Fig. 10 and Table 4) were measured using Gaussian 09 software. Chemical systems's initial ionization and electron affinity are determined by the negative orbital

energies of HOMO and LUMO below the Fermi level. HOMO and LUMO, as well as the band gap energy, are shown in a 3D frontier molecular orbital (FMOs) image. Fig. 11 depicts the HOMO and LUMO distributions of Cd-ZnO calculated using the B3LYP/6-31G level. A high band difference exists in the semiconductor ZnO nanoclusters. The HOMO and LUMO are concentrated on the Cd atoms in the Cd-ZnO system, indicating that Cd doping enables the formation of new energy levels closer to the Fermi level. Cd-ZnO has a HOMO and LUMO energy of -5.7210 and -3.3650 eV, respectively, and an E_g of 2.3560 eV. Red and green depict the positive and negative phases, respectively. The difference in energy between HOMO and LUMO may be used to calculate the optical band gap energy. Cd-ZnO clusters have lower band gap energy than ZnO NPs, implying that they are less stable and need less energy to excite an electron from the HOMO to the LUMO state. The theoretical calculated findings are closely related to the Tauc's plot, where Cd-ZnO NPs are attributed for the low band difference and red shift (Fig. 7). The Mulliken charge values were quantified using the B3LYP/6-31G levels of theory. Table 4 shows the Mulliken atomic charges in Cd-ZnO. The oxygen atoms in Cd-ZnO clusters have a negative charge, indicating that they are donor atoms. The positive charge of Zn and Cd atoms in Cd-ZnO clusters make them acceptor atoms. The reactivity and active site of the
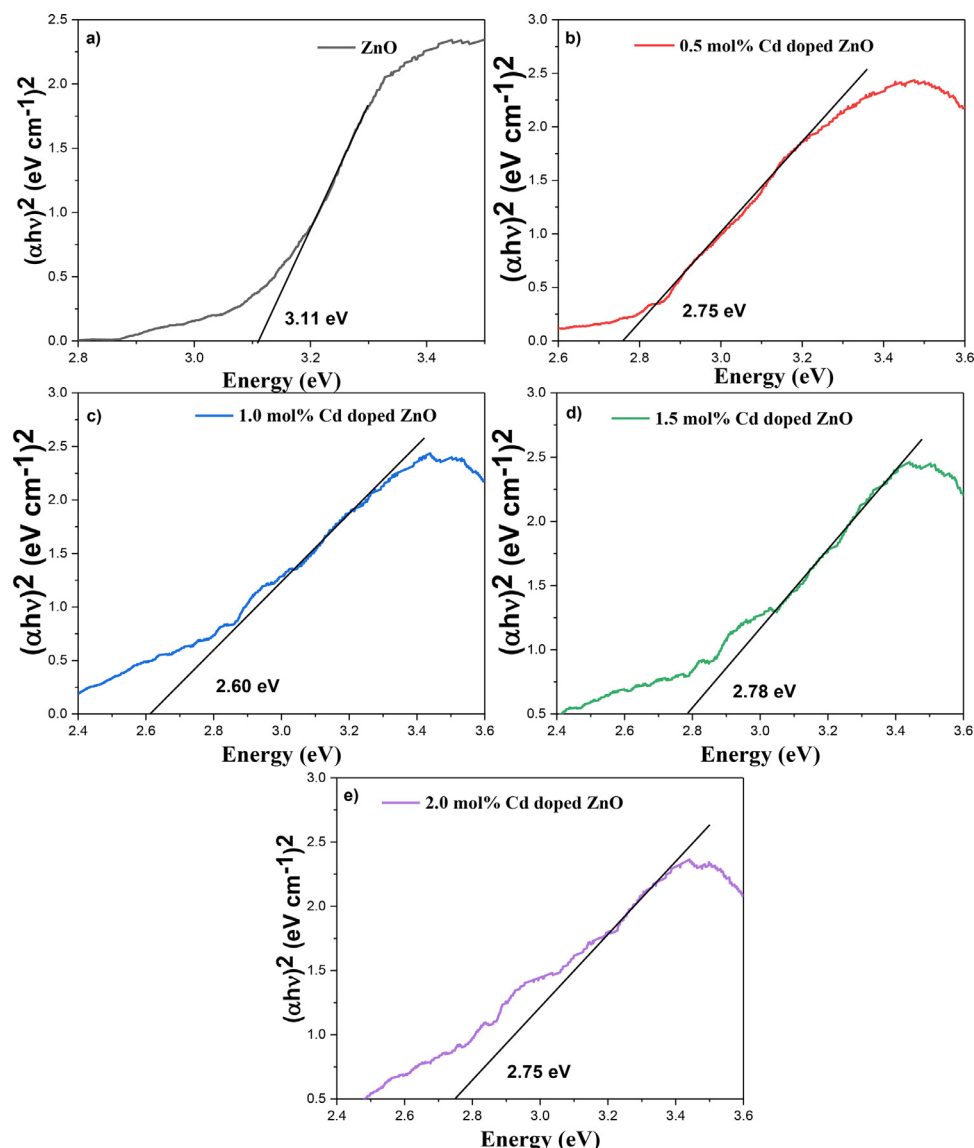
M.F. Sanakousar, Vidyasagar. C.C, Victor M. Jiménez-Pérez et al.

Journal of Hazardous Materials Advances 2 (2021) 100004

Fig. 7. Tauc's plot of undoped ZnO (a), 0.5 mol % Cd doped ZnO (b), 1.0 mol % Cd doped ZnO (c), 1.5 mol % Cd doped ZnO (d) and 2.0 mol % Cd doped ZnO.

Table 4
Theoretical results of ZnO and Cd-ZnO compound.

	ZnO	Cd-ZnO
HOMO	-0.21024	-0.21024
-0.16977		-0.12366
E_{HOMO} (eV)	-5.721	-5.721
E_{LUMO} (eV)	-2.6029	-3.365
EHOMO - ELUMO gap (eV)	3.1181	2.356
Ionization Potential (I) (eV)	6.9779	5.721
Electron affinity (A) (eV)	4.6197	3.365
Global hardness (η)	1.1791	1.178
Global Softness (S)	0.5895	0.589
Chemical potential (μ)	-5.7988	-4.543
Electro negativity (χ)	5.7988	4.543
Electrophilicity index (ω)	14.2594	8.7601
Mulliken atomic charges		
O		-0.468403
Zn		0.230170
Cd		0.238234

compounds are determined by the HOMO and LUMO energies. Negative chemical potential readings indicate that the molecule is spontaneously disintegrating. The compound's chemical hardness was determined to be 1.17 eV, and its high negative chemical potential (-4.54 eV) implies softness and high polarizability, as well as the fact that it decomposes spontaneously. The high levels of electronegativity and electrophilicity indicate that it has an impact on withdrawing electrons.

3.6. Photocatalytic experiment

UV-Visible absorption spectra obtained during CV degradation in aqueous solution at ambient temperature were utilized to investigate the photocatalytic activity of Cd-ZnO nanostructures. Before each exposure, a stirred combination of dye solution and catalyst was placed in the dark for 1 hour to create equilibrium between the dye molecule's adsorption and desorption processes on the catalyst's surface. The dye solution containing photocatalyst was subjected to UV irradiation by 06 W mercury lamp and collected during irradiation at routine time intervals to determine photocatalytic behaviour. A sample (5 ml) was obtained at specific time intervals and centrifuged for 03 minutes at 2500 rpm to separate catalyst particles from the aqueous phase to determine the degree of decolorization.

3.6.1. Photocatalytic activity evaluation

In order to investigate the catalytic behavior of pure ZnO and Cd-ZnO NPs, photocatalytic degradation of the two chromophoric dyes, CV
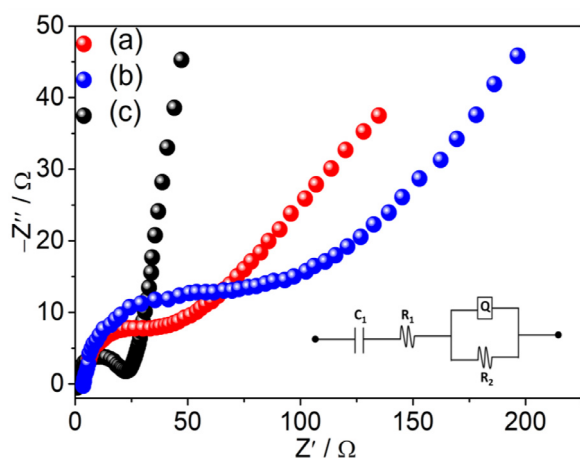
M.F. Sanakousar, Vidyasagar. C.C, Victor M. Jiménez-Pérez et al.

Journal of Hazardous Materials Advances 2 (2021) 100004

Fig. 8. EIS data of modified electrode in 0.5 M H_2SO_4 Electrolyte solution: Inset (a) bare GCE, (b) GCE/ZnO and (c) GCE/MWCNTs/ ZnO.
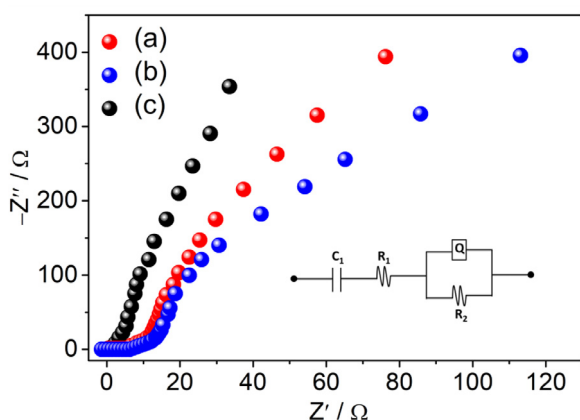

Fig. 9. EIS data of modified electrode in 0.5 M H_2SO_4 Electrolyte solution: Inset (a) bare GCE, (b) /GCE/0.5 mol% Cd-ZnO and (c) GCE/ MWCNTs/0.5 mol% Cd-ZnO.
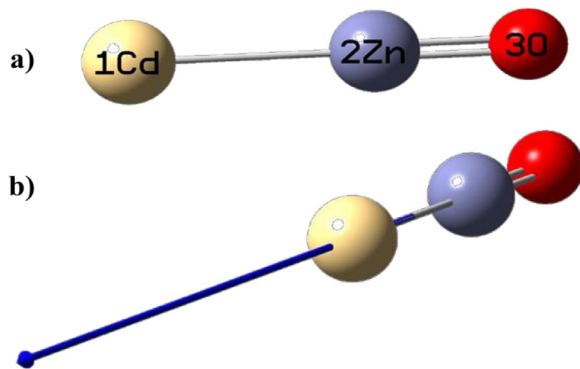

Fig. 10. Optimized structure of 0.5 mol% Cd-ZnO calculated at B3LYP/6-31G level of theory.

Fig. 11. Coloured 3D frontier molecular orbital (FMOs) diagram of HOMO-LUMO with ZnO band gap energy and 0.5 mol% Cd-ZnO.

(cationic dye) and Alizarine Red (anionic dye), with the 06 W (mercury-lamp) UV light irradiation at the same optimal conditions was used. CV and AR at 663 and 560 nm respectively have been monitored using the characteristic absorption values of pure and doped ZnO NPs for photocatalytics. Fig. 12a and b demonstrate the percentage degradation rate of CV dye as a function of irradiation time for various Cd mol% doped ZnO NPs, as well as the variation of C/Co v/s irradiation duration, where Co is initial dye concentration and C is the dye concentration at the time of measurements. Fig. 13a shows the percentage degradation rate of
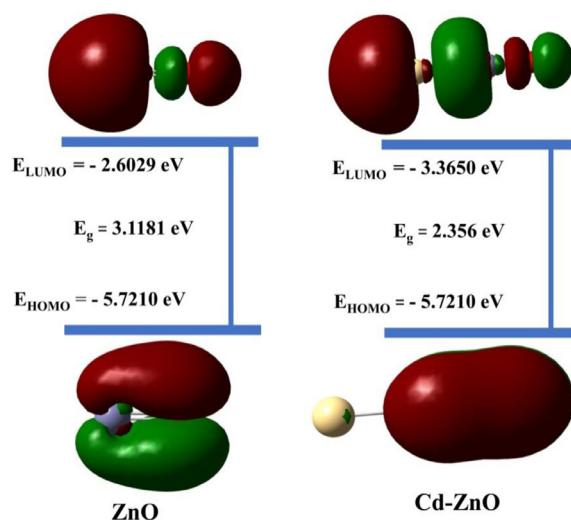
Alizarin Red S (ARS) dye with different Cd mol% doped ZnO NPs as a function of irradiation time. The results illustrated that, Cd-ZnO series NPs can degrade about 53 to 67% of ARS dye. Fig. 13b shows that a significant degradation rate was observed in the direct 06 W UV light in the absence of catalyst and the degradation rate was up to 84.0 % in 120 minutes. These results indicate that the Cd-ZnO series of compounds could be used effectively to degrade cationic dyes not anionic dyes. Samples of pure and Cd-ZnO were able to degrade CV dye as seen in a decrease in the characteristic absorption and decolouration, which showed that chromophoric dye groups were lost and converted to aromatic intermediates. Fig. 12a revealed that more than 80% of the dye is degraded within 120 minutes in the Cd-ZnO sequence of NPs. In comparison with higher doped concentrations Cd-ZnO and pure ZnO, major degradation of 0.5 mol% Cd-ZnO has been observed, with a dye degradation of about 94.67% over the same time. This rapid initial degradation by 0.5 mol% Cd-ZnO is an indication of the higher absorption coefficient of the doped NPs. The degradation profile indicates for cationic dyes that the higher concentration of Cd dopants is prohibitive as the Cd phase in the ZnO lattice (Fig. 12a and b and Table 2) and interfaces which make it possible to migrate from a localized to a non-localized charging centre. As a result, certain defect sites operate as active recombination centres for the electron-hole. Furthermore, photocatalysts are responsible for the agglomeration of particles and the changes in the size of the crystals.

3.6.2. Cd doping concentration effect

Fig. 12a shows the % degradation of CV over pure and different mol% of Cd-ZnO NPs, under 120 min illuminations. Results revealed that, the degradation of CV over Cd doped ZnO NPs follows the degradation order as 0.5 mol% > 0 mol% > 2.0 mol% >1.5 mol % >1.0 mol% Cd-ZnO NP's. The degradation efficiency of CV reaches 90.04% over 0.5 mol% Cd-ZnO in 90 min and 85.17% over pure ZnO, and 73.94% over 1.0 mol% Cd-ZnO, and 71.01% over 1.5 mol% Cd-ZnO, and 77.24% over 2.0 mol% Cd-ZnO NPs. As a result 0.5 mol% Cd implantation improves ZnO's photocatalytic activity in the photodegradation of CV, due to the increased charge separation potential (Table 5). Excessive Cd incorporation leads increase in electron-holes recombination rate, resulting in a loss in photocatalytic activity, and may possibly be attributed to the bulkiness of the presence of Cd-ZnO NPs. For reaching high degrading efficiency, 0.5 mol% Cd-ZnO NPs may be more effective. As the proportion of dopant in the photocatalyst increases, the efficiency of the photocatalyst decreases. This might be due to multiple trapping of charge carriers at higher dopant concentrations, such as 1.0 mol% (Cd), 1.5
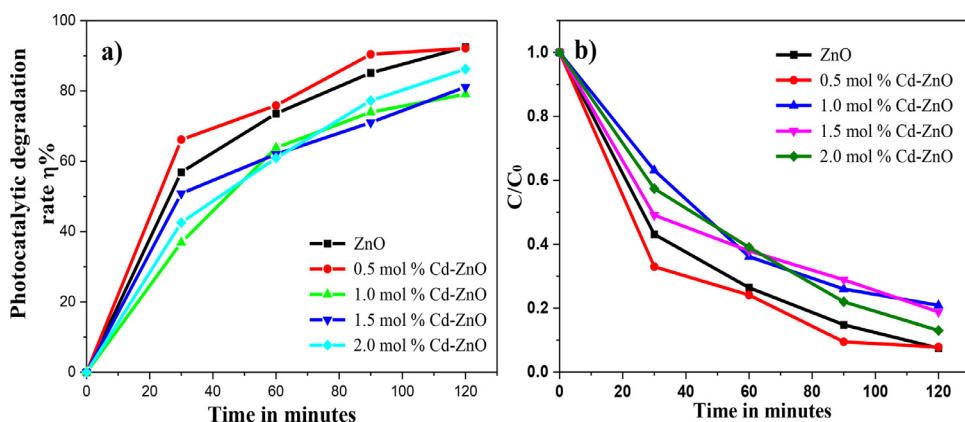
M.F. Sanakousar, Vidyasagar. C.C, Victor M. Jiménez-Pérez et al.

Journal of Hazardous Materials Advances 2 (2021) 100004

Fig. 12. (a) Plot of photocatalytic percentage degradation of CV being 10 mgL^{-1} with a catalyst dose of 0.010 gL^{-1} as a function of irradiation time and (b) Plot of (C/C$_0$) vs irradiation time for CV at different mol % Cd doped ZnO.
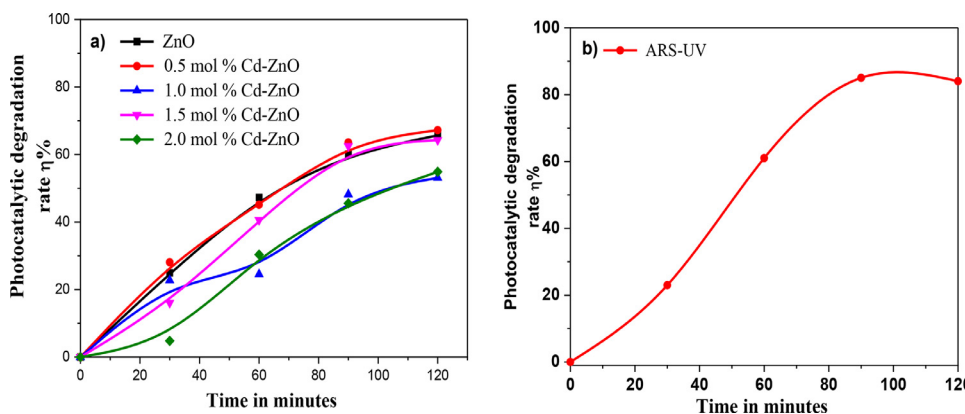

Fig. 13. Photocatalytic degradation rate % of ARS, [Catalyst] = 0.010 gL^{-1}, [ARS]= 10.0 mg L^{-1}, b) Photocatalytic degradation rate % of ARS only with UV without catalyst [ARS]= 10.0 mg L^{-1}, T=298K.

Table 5
Illustrates the effect of Cd doping, effect of dose and effect of pH in terms of percentage Degradation.

| Time (min) | % degradation | | | | | | | | | | | | | | |
| | Effect of Cd (%) | | | | | Effect of dose (mg) | | | | Effect of pH | | | | | |
	0	0.5	1	1.5	2	0.5	1	2	3	2	4	6	8	10	12
30	56.88	66.14	36.88	5.82	42.56	69.2	66.14	79.6	69.6	71.28	48.62	44.04	59.81	64.4	100
60	73.57	75.87	63.85	62.01	60.91	77.6	75.87	86.27	77.73	82.12	73.39	80	85.87	100	100
90	85.17	90.4	73.94	71.01	77.24	87.2	90.4	95.6	88.53	88.26	83.3	85.13	88.44	100	100
120	92.47	92.13	79.08	81.1	86.23	90.4	92.15	100	88.53	92.15	93.76	86.23	94.31	100	100

mol% (Cd), and 2.0 mol% (Cd), easier for recombination and only few charge carriers reaching the catalyst surface to initiate dye degradation. At higher Cd doping concentration, exhibit less photocatalytic activity due to the excessive Cd addition will cause photogenerated electrons and holes to recombine resulting in a decrease in photocatalytic activity, and may also due to the bulkiness of the presence of Cd on ZnO NPs. 0.5 mol % Cd-ZnO NPs may be more efficient for achieving high degradation efficiency (Li et al., 2014; Raza et al., 2016). Hence, the order of the photocatalytic activities of the Cd-ZnO with different Cd doping concentration is as follows 0.5 mol %> 0 mol % > 2.0 mol % >1.5 mol %>1.0 mol % Cd-ZnO NP's

3.6.3. Catalyst dose effect

The influence of catalyst dose on CV degradation was investigated using various amounts of catalyst ranging from 0.5 mg to 3.0 mg to optimize CV degradation efficiency while maintaining a CV concentration of 10.0 mg/L. Fig. 14 depicts the catalyst degradation efficiency of CV. Increased amounts of catalyst, ranging from 0.5 mg to 2.0 mg, resulted in increased photocatalytic degradation, indicating that the rate of degradation improves as the amount of catalyst increases. This could be because the number of active sites on the surface catalyst has increased. Hence the degradation depends on the amount of catalyst. However,

at a given agitation rate, the reaction mixture with a higher catalyst dose from 2.0 to 3.0 mg cannot be homogenised effectively; as a result, the active centres become inactive, leading to decreased catalytic activity. Because the higher catalyst dose blocks irradiation from penetrating into the solution, resulting in a reduction of catalytic activity. The rate of degradation of dye was almost constant when the amount of catalyst exceeds 2.0 mg. The 100% degradation was achieved with 0.5 mol % Cd-ZnO NPs in the same period (Adeel et al., 2021; Isai and Shrivastava, 2019).

3.6.4. pH effect

The pH is a most significant factor which can affect the degradation process of dye on the surface of the photocatalyst. By adding appropriate concentrations and volume of 0.1M H$_2$SO$_4$ and NaOH, the effects of different pH values ranging from 2.0 to 12.0 (acidic, neutral, and basic pH values) on dye degradation efficiency were investigated, and the findings were reported in Fig. 15. In an acidic media, CV degradation efficiency was found to be good, while in a basic media, it was found to be high. The degradation efficiency levels of CV were increased from 85.68% at pH 8.0 to 100% at pH 10.0 with the pure ZnO NPs and reaching 100 % in less than 60 minutes at pH 12.0. Whereas, 0.5 mol% Cd-ZnO degrades CV dye of about 94 % at pH 8, 100 % at pH 10 & 12
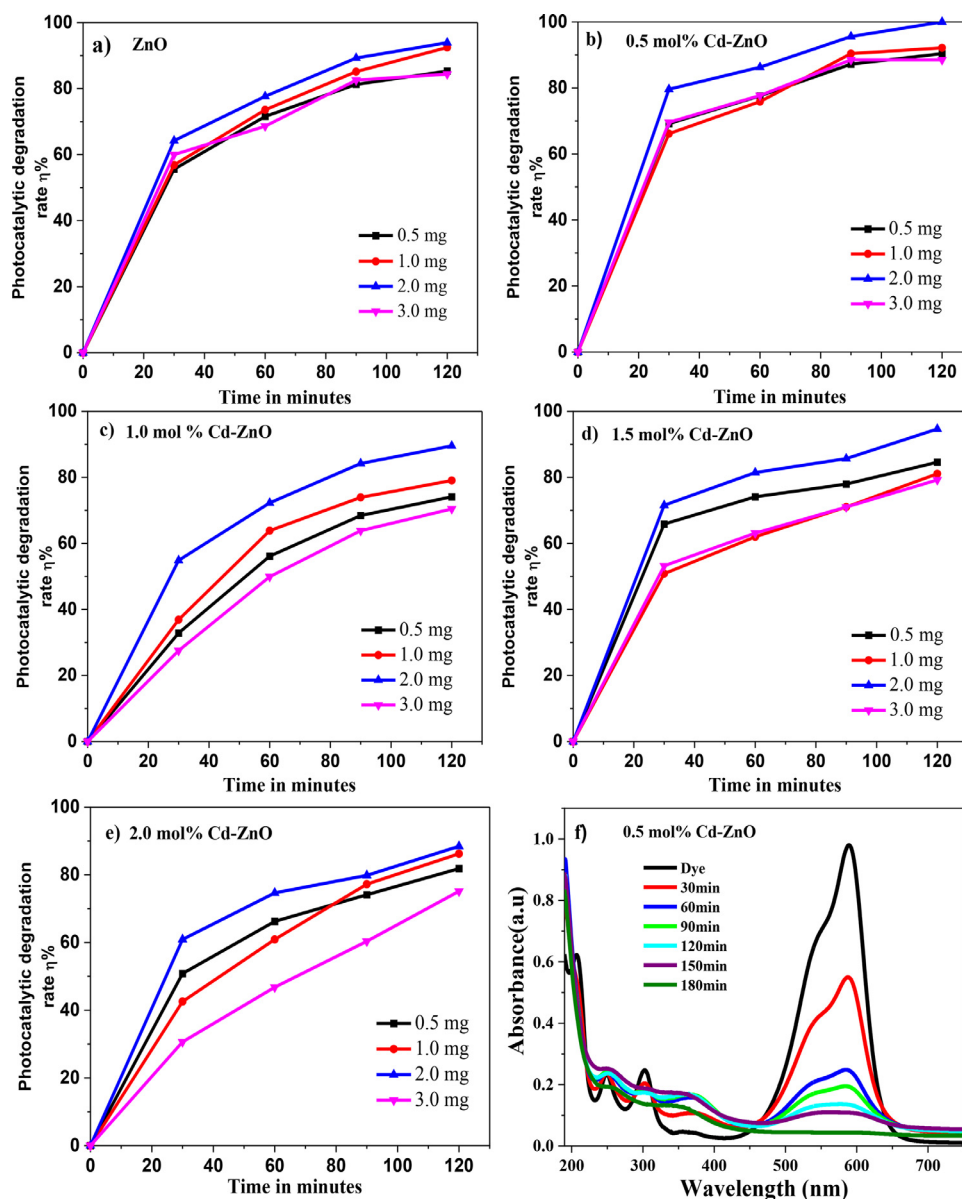
M.F. Sanakousar, Vidyasagar. C.C, Victor M. Jiménez-Pérez et al.

Journal of Hazardous Materials Advances 2 (2021) 100004

Fig. 14. Catalyst dose effect on the CV photodegradation rate with concentration of CV being 10 mg L^{-1} at different mol % Cd doped ZnO. (a) undoped, (b) 0.5 mol % Cd, (c) 1.0 mol % Cd, (d) 1.5 mol% Cd and (e) 2.0 mol % Cd, f) UV-Vis spectra of Crystal violet dye degradation.

Table 6
The rate constant values of the degradation process.

Catalyst load (mg/L)	0.5	1	1.5	2
K rate const x 10^{-2} / min ZnO	1.25	1.94	2.04	2.06
0.5 mol % Cd-ZnO	1.35	1.75	3.11	1.19
1.0 mol % Cd-ZnO	1.95	1.21	1.65	1
1.5 mol % Cd-ZnO	0.836	1.03	1.76	0.89
2.0 mol % Cd-ZnO	1.08	1.6	1.31	1.11
Initial conc. of dye mg/L	10	10	10	10

of Cd doping with 2 mg catalyst at pH 10 and 12 has a high degradation efficiency in 60 min and 30 min compared to 1.0, 1.5 and 2.0 mole % of Cd doped ZnO, respectively. The theoretical physicochemical properties of CV dyes are tabulated in Table 7.

3.6.5. Kinetics study

The rate of CV degradation by pure and doped series was confirmed by a fractional-order kinetics the rate constant can be determined by using following equation. This equation can be used to express the Langmuir-Hinshelwood equation (Singh et al., 2020).

$$lnC/C_o = -kt$$

Where K: represents rate constant of the photocatalytic reaction, C$_o$ is the initial concentration of the CV dye, and C is the concentration of CV at time *t*. Fig. 16 illustrated that the photocatalytic degradation of CV by the Cd-ZnO NPs confirms the fractional order reaction. All the R correlation coefficient values were found to be 0.9858, 0.8914, 0.9939, 0.8796 and 0.9995 shows higher than 0.9 for pure ZnO, 0.5 mol % Cd-ZnO, 1.0 mol % Cd-ZnO, 1.5 mol % Cd-ZnO and 2.0 mol % Cd-ZnO photocatalysts respectively (Fig. 16), but 2 mg of photocatalyst has more effective and maximum degradation. This confirms the fractional
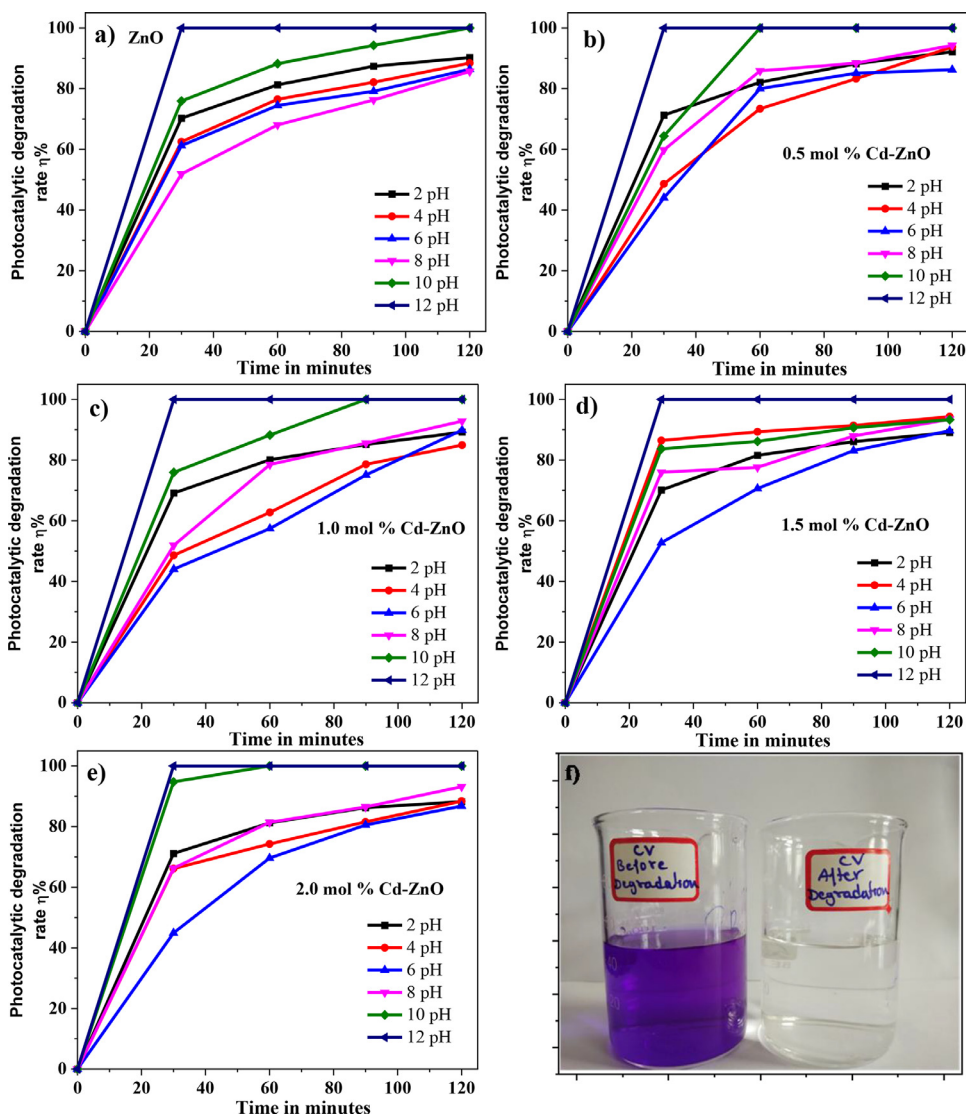
in 60 & 30 minutes, respectively. Due to the intense bonding between OH and metal at alkaline pH, the photocatalyst surface is negatively charged at high pH, and the dye cations were electrostatically drawn further towards the catalyst surface as the number of reducing electrons increased, resulting in good CV dye degradation. At alkaline pH, hydroxyl radicals are the most common species. Since, the dye concentration has decreased whereas the amount of ·OH has increased. As a result, attacks by these radicals with a high oxidation potential occur more frequently (Isai and Shrivastava, 2019; Kenchappa Somashekharappa and Lokesh, 2021). From Tables 5 and 6 it is clearly indicates that 0.5 mol %

Fig. 15. pH effect on the CV photodegradation rate with concentration of CV being 10 mgL^{-1} at different mol% Cd doped ZnO.

order kinetic model for CV photocatalytic degradation and that the slope of the linear curve is rate constant *k*. The rate constant values of the degradation process were calculated and presented in Table 6.

3.6.6. In situ capture experiment

According to literature, super oxide and hydroxyl radicals, as well as holes generated in the photocatalytic reactions, have a significant impact on the degradation of organic pollutants. In order to better understand the mechanism of photocatalytic degradation of CV dye in the presence of Cd-ZnO NPs. Different scavengers are used to trap active species in order to identify the species responsible for CV degradation (Fig. 17). 1 mM t-Butanol, p-Benzoquinone and EDTA-2Na were used as a scavengers in this study to remove$^{•}$OH, O$_2$$^{•-}$ and h$^+$ respectively. With the addition of these three scavengers, the degradation rate is reduced. p-Benzoquinone (super oxide radical scavenger) had only a minor effect on the dye degradation rate, indicating that the super oxide radical is not the primary reactive species in the dye degradation process. EDTA-2Na (holes scavenger) had a minor effect on degradation process, implying that holes were secondary reactive species. However, adding t-Butanol (hydroxyl radical scanvenger), reduced the dye degradation significantly, suggesting that hydroxyl radical is the primary reactive species in the dye degradation process. The percentage of reactive species is as follows: t-Butanol (27.75%), EDTA-2Na (39.14%) and p-Benzoquinone (48.75%). As a result, hydroxyl radical and holes are reac-

tive species than super oxide radicals in the photocatalytic degradation of CV dye (Zheng et al., 2019; Mirzaeifard et al., 2020; Ghoderao et al., 2019).

3.6.7. Photocatalytic degradation mechanism

From Fig. 18 we propose a possible mechanism for the photocatalytic degradation based on scavenger experiments. Three important steps are involved in the photocatalytic degradation process. The first is charge separation, the valence band (VB) holes (h$^+$) and conduction band (CB) electrons (e$^-$) are generated when the energy from UV light falls on the surface of Cd-ZnO, separating the electron and hole. Second, the excited electrons are transffered to the surface of Cd while holes remains in the ZnO, as a consequence, doping with Cd metal slows down the recombination. The photocatalytic activity is effectively increased by preventing electron-hole pair recombination. Third there is, the redox process which invloves the reaction of electrons. The Cd^{2+} trap electrons from the ZnO's CB and convert them to Cd$^+$. Becauase the Cd$^+$ ion is so unstable, it reacts with an oxygen molecule to form Cd^{2+} ion with super oxide radical. The Cd possess a +2 oxidation state and a 4d^{10} electronic configration, which is stable. The stable electronic configration of the Cd^{2+} is distributed as it traps the electron. As a result, the trapped electrons are finally transffered to an oxygen molecule, resulting in superoxide radicals and the hole in the ZnO NPs. The highly reactive hydroxyl radicals are formed when photoinduced holes in ZnO's VB react with
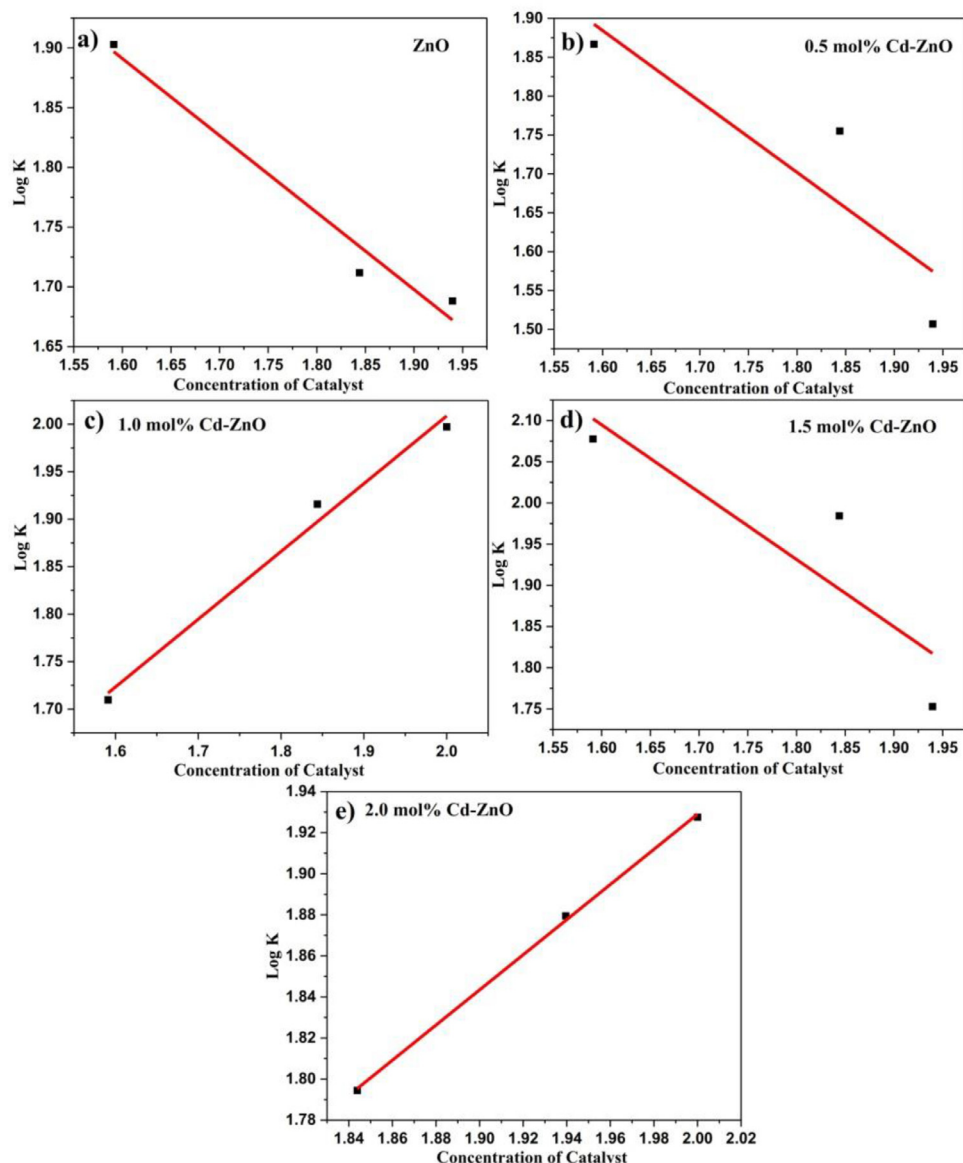
Fig. 16. A plot of rate constant verses concentration of catalyst.

water molecules or surface hydroxyl groups. Highly reactive hydroxyl radicals are responsible for the degradation of CV dye and the possible steps are given below (Phuruangrat et al., 2015; Ghoderao et al., 2019; Zhang and Zeng, 2012; Khayyat et al., 2012; Zhai et al., 2014; Dumrongrojthanath et al., 2021).
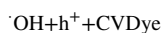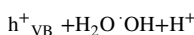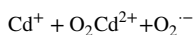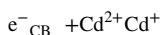
The possible mechanism

$$ZnO + h\nu \; e^-_{CB} + h^+_{VB}$$

$$e^-_{CB} + Cd^{2+} Cd^+$$

$$Cd^+ + O_2 Cd^{2+} + O_2^{\cdot-}$$

$$h^+_{VB} + H_2O \; ^{\cdot}OH + H^+$$

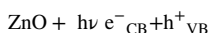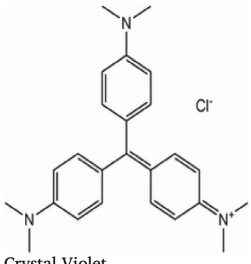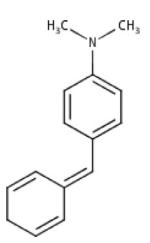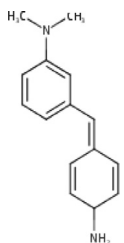$$H^+ + OH^- \; ^{\cdot}OH$$

$$^{\cdot}OH + h^+ + CVDye$$

Fig. 14f shows the UV-Visible spectra of CV dye solution as a function of reaction time for 0.5 mol% Cd-ZnO. At the start of the experiment, prior to the oxidation process, the absorption spectrum of CV in water was characterized by primary peak in the visible region (584 nm) and two secondary peaks in the UV region (250 and 300 nm), as shown in these spectra. The chromophore was attributed to the peak at 584 nm, whereas the aromatic structures of the molecules were assigned to the peaks at 250 and 300 nm (He et al., 2010; Abbas et al., 2020). The apparent peaks faded with time due to the oxidative cleavage of the aromatic rings. The breakdown of the dye molecule and its intermediates was thought to be indicated by a decrease in absorbance at 250 and 300 nm.

3.6.8. Photocatalyst stability

By exposing the catalyst to five photodegradation experiments with the same concentration of CV dye and measuring percentage degradation, the stability of the photocatalyst sequence pure ZnO and different Cd mol% doped ZnO was assessed to determine the degradation efficiency of the catalyst. The catalyst was washed with deionized water and alcohol after each degradation step to eliminate any adsorbed CV on the surface, and then dried in an oven. Fig. 19 shows that the

Table 7
Theoretical physicochemical properties of before and after degraded dye products.

| Physicochemical properties	Crystal Violet	Degraded Products	
Formula	$C_{25}H_{30}ClN_3$	$C_{15}H_{17}N$	$C_{15}H_{18}N_2$
Molecular weight	407.98 g/mol	211.30 g/mol	226.32 g/mol
Num. heavy atoms	29	16	17
Num. arom. heavy atoms	12	6	6
Fraction Csp3	0.24	0.2	0.2
Num. rotatable bonds	4	2	2
Num. H-bond acceptors	0	0	1
Num. H-bond donors	0	0	1
Molar Refractivity	128.45	71.71	74.42
TPSA	9.49 Å^2	3.24 Å^2	29.26 Å^2
Log Po/w (iLOGP)	-3.09	2.98	2.65
Log S (ESOL)	-2.88	-3.75	-2.96
Solubility	–	3.79e-02 mg/ml ; 1.79e-04 mol/	2.48e-01 mg/ml ; 1.10e-03 mol/l
Class	Soluble	Soluble	Soluble
Log S (Ali)	-0.52	-3.66	-2.78
Solubility	–	4.67e-02 mg/ml ; 2.21e-04 mol/l	3.75e-01 mg/ml ; 1.66e-03 mol/l
Class	Soluble	Soluble	Soluble
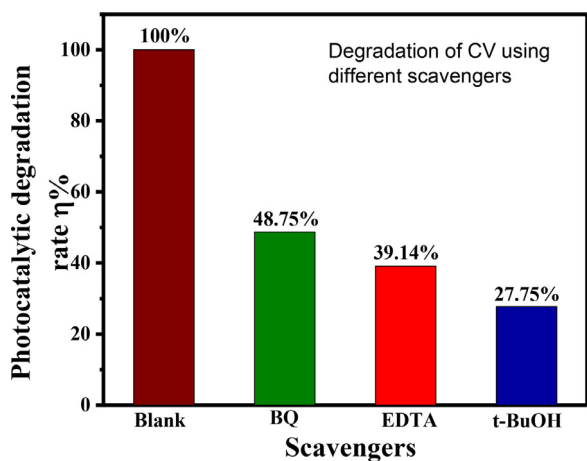
Fig. 17. Effect of scavengers on degradation of CV using BQ for super oxides, EDTA for holes and t-BuOH for hydroxyl radicals.
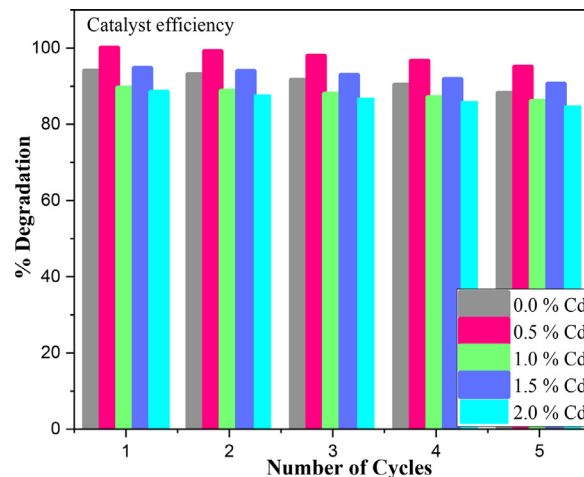

Fig. 19. Photocatalytic stability of Cd-ZnO crystals at different Cd doping concentration with Crystal violet.
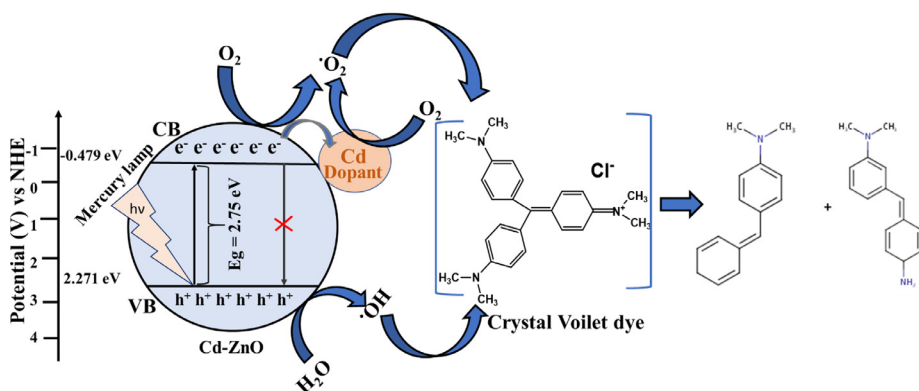
Fig. 18. Photocatalytic degradation mechanism of CV using Cd-ZnO NPs at 06 Watt.
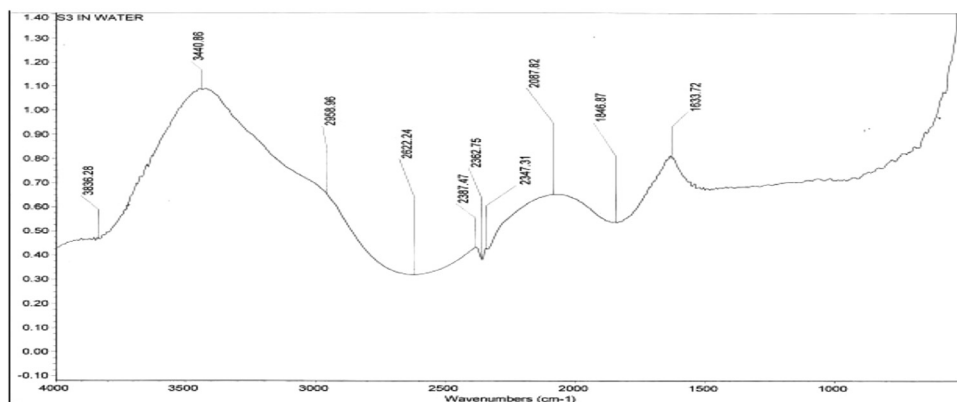
M.F. Sanakousar, Vidyasagar. C.C, Victor M. Jiménez-Pérez et al.

Journal of Hazardous Materials Advances 2 (2021) 100004

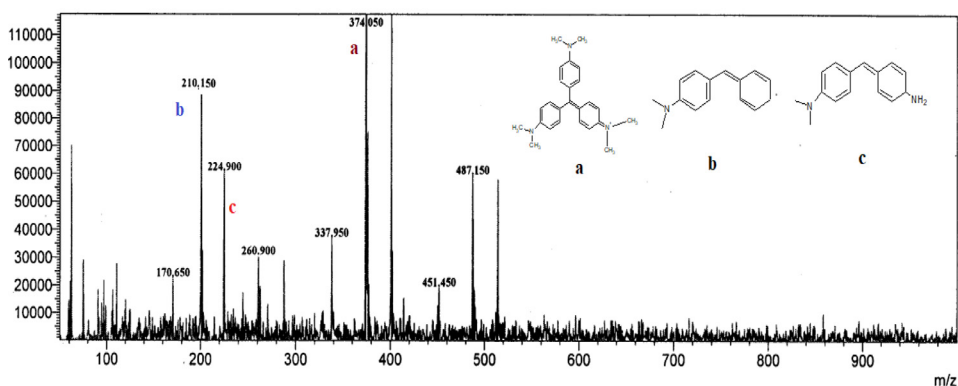**Fig. 20.** FTIR analysis of degraded CV dye solution.

Fig. 21. Mass spectra of CV dye's possible fragmentations generated using 0.5 mol% Cd-ZnO catalyst after degradation.

photocatalyst exhibited significant stability even after five cycles, with a maximum CV degradation of 88.12 %, 95.0 %, 86.0 %, 90.54 %t, and 84.84 %, respectively, with pure ZnO to different Cd mol% doped ZnO. The loss of the photocatalyst due to washing between cycles may explain the decrease in degradation efficiency. Because of the photocatalyst's stability, it can be reused several times, lowering the expense of effluent treatment (Jayaraman et al., 2020). Table 9 comparing the maximal degradation capacities (%) of crystal violet (Abbas et al., 2020; Djellabi et al., 2015; Rao Akshatha et al., 2020; Li et al., 2020; Lin et al., 2016; Ma et al., 2018; Cherrak et al., 2020; Bargozideh and Tasviri, 2018; Vinosel et al., 2019; Sharma et al., 2012; Mittal et al., 2014; Mohamed et al., 2018; Dargahi et al., 2020; Ahmad et al., 2021; Kossar et al., 2020; Rahmat et al., 2019) with literature degradation percent values for other catalysts. The maximal degradation capacities of Cd-ZnO for crystal violet at 30 minutes are greater than those of other materials, which might be related to Cd-ZnO nanoparticles' larger specific surface and band gap alignment (Table 10).

4. FTIR and Mass spectra analysis

Remarkable evidence for the complete oxidative cleavage of the dye was observed in both functional group and fingerprint region (4000 to 400 cm^{-1}) of degraded CV dye. Form literature IR spectrum of untreated dye absorption peak at 1583 cm^{-1} (C=C stretching) indicate presence of mono-substituted and para-disubstituted benzene rings, peaks at 1164 cm^{-1} (C-N Stretching aromatic amine) and 2920 cm^{-1} (Alkene C–H stretching) respectively (Abdi et al., 2020; Ameen et al., 2013). Spectrum of degraded CV dye sample has shown greater variation as breaking of the various functional groups and distracting the various bond of the dye molecule after exposing to 06 Watt UV lamp using 0.5 mol%
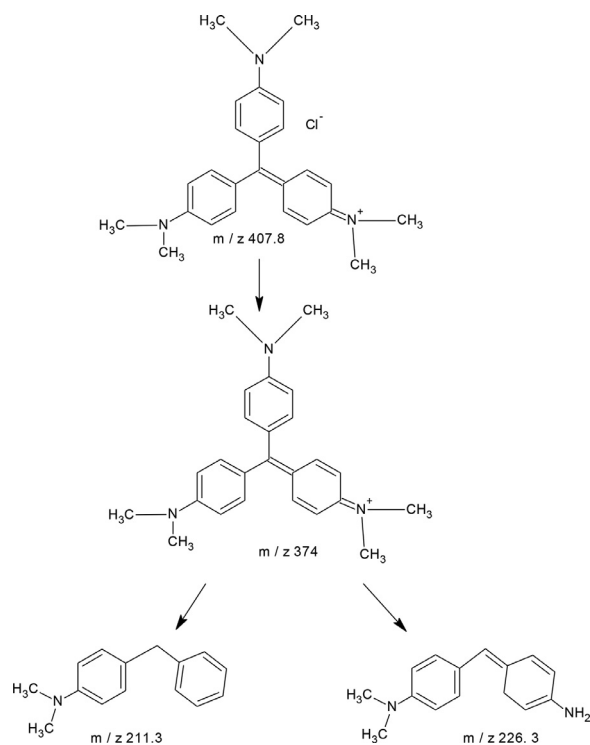

Fig. 22. Possible reaction intermediates after the photocatalytic reaction using 06 Watt UV light illumination.

Table 8

Prediction of eco-toxicity based on LC_{50} and IGC_{50} using toxicity estimation software tool (TEST), developed by the US Environmental Protection Agency.

Compounds		EPA-TEST (Consensus method)			EPA-CompTox Chemicals Dashboard (Consensus method)		
		Fathead minnow (96 hr)	D.magna LC$_{50}$ (48 hr)	T. pyriformis IGC$_{50}$ (48 hr)	Fathead minnow (96 hr)	D.magna LC50 (48 hr)	T. pyriformis IGC$_{50}$ (48 hr)
C1	-Log10(mol/L)	5.27	5.14	N/A	N/A	N/A	N/A
	mg/L	2.05	2.8	N/A	N/A	N/A	N/A
TM1	-Log10(mol/L)	4.74	5.29	4.41	4.95	5.22	4.51
	mg/L	3.95	1.1	8.42	2.423	1.311	6.589
TM2	-Log10(mol/L)	5.41	5.07	5.02	4.96	5.53	5.01
	mg/L	0.91	2.0	2.23	2.524	0.675	2.23

Dye molecule: C1; Transformed molecule I: TM1; Transformed molecule II: TM2; N/A: Not available.

Table 9

Comparison of maximum degradation capacities of CV dye using different catalysts.

Catalysts	Methods of preparation	Degradation %	Irradiation source	Irradiation Time (min)	Ref.
TiO$_2$ Montmorillonite	Impregnation method	97.1	UV light	350	54
Fe$_3$O$_4$/SnO$_2$	Hydrothermal method	83	UV	180	55
Fe$_3$Se$_4$ & Bi$_2$Se$_3$ Composites with chitosan	Solvothermal process	100	Sunlight	150	60
Ga$_2$Zr$_2$-$_x$W$_x$O$_7$	Pechini method	100	Visible light	300	53
Gadolinium doped bismuth ferrite (Gd:BFO)	Auto combustion method	84.5	Visible light	180	61
3D MnO$_2$ nanofibrous mesh	Hydrothermal method	97	Visible light	90	62
MoS$_2$/Wurtzite ZnS	Hydrothermal method	98.5	Visible light	40	63
Ag$_2$S/PbBiO$_2$Br	Hydrothermal method	94.4	Visible light	60	64
SrFeO$_{3-x}$/g-C$_3$N$_4$	Sintering method	95	Visible light	720	65
Ag$_3$PO$_4$/Bi$_2$WO$_6$-0.3	Hydrothermal method	90	Visible light	180	66
Nano TiO$_2$/Diatomite composite	Sol-gel method	99.17	UV light	735	67
BiSI/MoS$_2$	Hydrothermal method	80	Visible light	240	68
TG capped ZnS	Precipitation method	87	Visible light	180	56
Mn dopped and PVP capped ZnO NP's	Precipitation method	100	UV- Visible light	180	57
Grafted sodium alignate/ZnO/GO	Hummer's method	94	Sunlight	300	58
Ce$_2$(MoO$_3$)$_4$	Microemulsion method	89	Visible light	300	59
0.5 mol% Cd doped ZnO	Precipitation method	100	UV Chamber (06 W)	30	Present work

Cd-ZnO catalysts (Fig. 20). Broad peak at about 3836 cm^{-1} (OH stretching) is assigned for stretching vibration of OH group of water molecule. The absorption peak at about 2362 cm^{-1}(N-H stretching) and absence of 1360 cm^{-1}(C=N) IR confirms the degradation of C=N into primary amine. Literature report reveals that molecular mass of the CV dye was found to be m/z 407.9. Mass spectrum of the degraded CV dye shown strong prominent signal at m/z 374, 224.9 and 210.1 multiple signals in mass spectrum confirms the multiple reaction intermediates due to breaking of the bonds (Fig. 21) and path way of degradation is shown in Fig. 22.

5. In silico eco-toxicity analysis

The EPA-TEST and EPA-CompTox Chemicals Dashboard were employed for the prediction of the eco-toxicity end points of the chemical compounds in this study. *Fathead minnow, D. magna* and *T. pyri-*formis were considered to predict and analyse the eco-toxicity levels based on the 50% lethal concentrations (LC_{50}) and the results were compiled in Table 8. Based on the prediction results we can note that the molecule (C1) and transformed molecule (TM2) exhibited eco-toxicities in the similar order of scale in the TEST prediction whereas the transformed molecule TM1 showed slightly high toxicity in Fathead minnow comparatively. In case of Computational Toxicology (CompTox) Chemicals Dashboard (Grulke et al., 2019; Ferri et al., 2017) the predicted values of C1 were unavailable. Further prediction of TM1 and TM2 molecules in *D. magna* LC_{50} (48 hr) yielded highly conserved scale of order indicating lower toxicity, in comparison with fish as expected. Prediction of T. *pyriformis* IGC_{50} (48 hr) resulted in varied toxicity levels in TM1 and TM2 where TM2 exhibited low toxicity. By the application of both the EPA TEST program and the knowledgebase demonstrated TM2 to be relatively less eco-toxic compared with C1 and TM1.

Table 10

Comparison of maximum degradation capacities of different dyes using Cd-ZnO catalysts.

Cd-ZnO with concentration	Process condition	Pollutant	Irradiation source	Degradation %	Irradiation time (min)	Ref.
(4%) Cd-ZnO	Dose: 20 mg Conc.: – (50 ml)	MB	Sunlight	84	30	(Ghoderao et al., 2019)
Cd-ZnO	Dose: 0.04g/L Conc. 10ppm	MB	Visible light	80	200	(Zhang and Zeng, 2012)
Cd-ZnO	Dose:150 mg Conc.: 0.3 M	AO (Acridine orange)	UV (250 W)	92.4	90	(Khayyat et al., 2012)
(3%) Cd-ZnO	Dose: 0.2 g Conc.: 1^*10^{-5} mol/L (100ml)	MB	UV (18 W)	89	240	(Dumrongrojthanath et al., 2021)
(5%) Cd-ZnO	Dose: 90 mg Conc.:5^*10^{-5} M (100 ml)	RhB	UV (9 W)	98	180	(Zhai et al., 2014)
(0.5%) Cd-ZnO	Dose: 2 mg Conc.: 10 ppm (50 ml)	CV	UV (6 W)	100	30	Present Study

6. Conclusions

We reported our complete characterizations of the Cd-ZnO catalyst in this paper to make researcher more aware of the mechanism of Cd-ZnO's improved photodegradation efficiency. This work describes the ZnO and various mol% Cd doped ZnO photocatalysts for CV degradation. The implantation of Cd into the ZnO lattice was confirmed using XRD, EDAX, UV-Vis spectroscopy, and quantum theoretical measurements using density function theory. Because the fundamental crystal size, band gap, carrier separation and transfer performance are considered to be the most important elements impacting Cd-ZnO's photoactivity. The photocatalytic degradation of crystal violet demonstrated that 0.5 mol% Cd implantation considerably improved ZnO photocatalytic activity. After Cd doping, optical band gap of ZnO was modified, resulting in $\cdot O_2^-$ production and a significant increase in photodegradation. Mulliken atomic charges and molecular characteristics were determined at the B3LYP/6-31G level of theory. The HOMO-LUMO band gap of alleged photocatalysts was calculated using density function theory. The influence of experimental factors such as catalyst recycling, catalyst dosage, and pH on photocatalytic activity was investigated. The US Environmental Protection Agency's Toxicity Estimation Software Tool (TEST) was used to calculate the toxicity of degraded CV dye. After 30 minutes at pH 10-12, mass spectroscopy confirms that CV-dye has completely degraded and divided into small mass signals. These results propose that the Cd-ZnO compounds might be employed to breakdown cationic dyes successfully. The increased electrochemical and photocatalytic performance of these nanocomposites suggests that they have dual activity in waste water treatment and energy applications.

Declaration of Competing Interest

There are no conflicts to declare.

Acknowledgement

References

Aqeel, M., Rashid, M., Ikram, M., Haider, A., Naz, S., Haider, J., Ul-Hamid, A., Shahzadi, A., 2020. Photocatalytic, dye degradation, and bactericidal behavior of Cu-doped ZnO nanorods and their molecular docking analysis. Dalton Trans. 49, 8314–8330. doi:10.1039/d0dt01397h.

Yuan, Z., Wang, J., Wang, Y., Liu, Q., Zhong, Y., Wang, Y., Li, L., Lincoln, S.F., Guo, X., 2019. Preparation of a poly(acrylic acid) based hydrogel with fast adsorption rate and high adsorption capacity for the removal of cationic dyes. RSC Adv. 9, 21075–21085. doi:10.1039/c9ra03077h.

Spitaleri, L., Nicotra, G., Zimbone, M., Contino, A., Maccarrone, G., Alberti, A., Gulino, A., 2019. Fast and efficient sun light photocatalytic activity of Au_ZnO core-shell nanoparticles prepared by a one-pot synthesis. ACS Omega 4, 15061–15066. doi:10.1021/acsomega.9b01850.

Mittal, M., Sharma, M., Pandey, O.P., 2014. UV-visible light induced photocatalytic studies of Cu doped ZnO nanoparticles prepared by co-precipitation method. Sol. Energy 110, 386–397. doi:10.1016/j.solener.2014.09.026.

Jayaraman, V., Ayappan, C., Palanivel, B., Mani, A., 2020. Bridging and synergistic effect of the pyrochlore like $Bi_2Zr_2O_7$ structure with robust CdCuS solid solution for durable photocatalytic removal of the organic pollutants. RSC Adv. 10, 8880–8894. doi:10.1039/d0ra00644k.

Zhu, H., Jiang, R., Xiao, L., Chang, Y., Guan, Y., Li, X., Zeng, G., 2009. Photocatalytic decolorization and degradation of Congo Red on innovative crosslinked chitosan/nano-CdS composite catalyst under visible light irradiation. J. Hazard. Mater. 169, 933–940. doi:10.1016/j.jhazmat.2009.04.037.

Ghosh, S., Kouamé, N.A., Ramos, L., Remita, S., Dazzi, A., Deniset-Besseau, A., Beaunier, P., Goubard, F., Aubert, P.H., Remita, H., 2015. Conducting polymer nanostructures for photocatalysis under visible light. Nat. Mater. 14, 505–511. doi:10.1038/nmat4220.

Dâas, A., Hamdaoui, O., 2010. Extraction of anionic dye from aqueous solutions by emulsion liquid membrane. J. Hazard. Mater. 178, 973–981. doi:10.1016/j.jhazmat.2010.02.033.

El-Naas, M.H., Al-Muhtaseb, S.A., Makhlouf, S., 2009. Biodegradation of phenol by Pseudomonas putida immobilized in polyvinyl alcohol (PVA) gel. J. Hazard. Mater. 164, 720–725. doi:10.1016/j.jhazmat.2008.08.059.

Zhang, D.Y., Li, W.G., Zhang, S.M., Liu, M., Zhao, X.Y., Zhang, X.C., 2011. Bacterial community and function of biological activated carbon filter in drinking water treatment. Biomed. Environ. Sci. 24, 122–131. doi:10.3967/0895-3988.2011.02.006.

Gomes, H.T., Machado, B.F., Ribeiro, A., Moreira, I., Rosário, M., Silva, A.M.T., Figueiredo, J.L., Faria, J.L., 2008. Catalytic properties of carbon materials for wet oxidation of aniline. J. Hazard. Mater. 159, 420–426. doi:10.1016/j.jhazmat.2008.02.070.

Xie, J., Wen, W., Jin, O., Xiang, X.B., Wu, J.M., 2019. TiO2 nanotrees for the photocatalytic and photoelectrocatalytic phenol degradation. New J. Chem. 43, 11050–11056. doi:10.1039/c9nj02219h.

Chen, Y., Xiang, Z., Wang, D., Kang, J., Qi, H., 2020. Effective photocatalytic degradation and physical adsorption of methylene blue using cellulose/GO/TiO2 hydrogels. RSC Adv. 10, 23936–23943. doi:10.1039/d0ra04509h.

Chimupala, Y., Phromma, C., Yimklan, S., Semakul, N., Ruankham, P., 2020. Dye wastewater treatment enabled by piezo-enhanced photocatalysis of single-component ZnO nanoparticles. RSC Adv. 10, 28567–28575. doi:10.1039/d0ra04746e.

Zhang, P., Xu, J., Wang, X.J., He, B., Gao, S.Q., Lin, Y.W., 2019. The third generation of artificial dye-decolorizing peroxidase rationally designed in myoglobin. ACS Catal. 9, 7888–7893. doi:10.1021/acscatal.9b02226.

Wang, X.J., Yang, W.Y., Li, F.T., Bin Xue, Y., Liu, R.H., Hao, Y.J., 2013. In situ microwave-assisted synthesis of porous N-TiO2/g-C3N4 heterojunctions with enhanced visible-light photocatalytic properties. Ind. Eng. Chem. Res. 52, 17140–17150. doi:10.1021/ie402820v.

Kong, W., Wang, S., Wu, D., Chen, C., Luo, Y., Pei, Y., Tian, B., Zhang, J., 2019. Fabrication of 3D sponge@AgBr-AgCl/Ag and tubular photoreactor for continuous wastewater purification under sunlight irradiation. ACS Sustain. Chem. Eng. 7, 14051–14063. doi:10.1021/acssuschemeng.9b02575.

M.F. Sanakousar, Vidyasagar. C.C, Victor M. Jiménez-Pérez et al.

Journal of Hazardous Materials Advances 2 (2021) 100004

Sakib, A.A.M., Masum, S.M., Hoinkis, J., Islam, R., Molla, M.A.I., 2019. Synthesis of CuO/ZnO nanocomposites and their application in photodegradation of toxic textile dye. J. Compos. Sci. 3, 91. doi:10.3390/jcs3030091.

Venkatesha, T.G., Arthoba Nayaka, Y., Viswanatha, R., Vidyasagar, C.C., Chethana, B.K., 2012. Electrochemical synthesis and photocatalytic behavior of flower shaped ZnO microstructures. Powder Technol. 225, 232–238. doi:10.1016/j.powtec.2012.04.021.

Boruah, P.K., Sharma, B., Karbhal, I., Shelke, M.V., Das, M.R., 2017. Ammonia-modified graphene sheets decorated with magnetic Fe₃O₄ nanoparticles for the photocatalytic and photo-Fenton degradation of phenolic compounds under sunlight irradiation. J. Hazard. Mater. 325, 90–100. doi:10.1016/j.jhazmat.2016.11.023.

Soltani, N., Saion, E., Hussein, M.Z., Erfani, M., Abedini, A., Bahmanrokh, G., Navasery, M., Vaziri, P., 2012. Visible light-induced degradation of methylene blue in the presence of photocatalytic ZnS and CdS nanoparticles. Int. J. Mol. Sci. 13, 12242–12258. doi:10.3390/ijms131012242.

Pirsaheb, M., Hossaini, H., Nasseri, S., Azizi, N., Shahmoradi, B., Khosravi, T., 2020. Optimization of photocatalytic degradation of methyl orange using immobilized scoria-Ni/TiO₂ nanoparticles. J. Nanostructure Chem. 10, 143–159. doi:10.1007/s40097-020-00337-x.

Neelgund, G.M., Oki, A., 2019. Cobalt phthalocyanine-sensitized graphene-ZnO composite: an efficient near-infrared-active photothermal agent. ACS Omega 4, 5696–5704. doi:10.1021/acsomega.8b03222.

Kiriarachchi, H.D., Abouzeid, K.M., Bo, L., El-Shall, M.S., 2019. growth mechanism of sea urchin ZnO nanostructures in aqueous solutions and their photocatalytic activity for the degradation of organic dyes. ACS Omega 4, 14013–14020. doi:10.1021/acsomega.9b01772.

Shafi, A., Ahmad, N., Sultana, S., Sabir, S., Khan, M.Z., 2019. Ag₂S-sensitized NiO-ZnO heterostructures with enhanced visible light photocatalytic activity and acetone sensing property. ACS Omega 4, 12905–12918. doi:10.1021/acsomega.9b01261.

Lavand, A.B., Malghe, Y.S., 2015. Synthesis, characterization, and visible light photocatalytic activity of nanosized carbon doped zinc oxide. Int. J. Photochem. 2015, 1–9. doi:10.1155/2015/790153.

Vidyasagar, C.C., Naik, Y.A., Venkatesh, T.G., Viswanatha, R., 2011. Solid-state synthesis and effect of temperature on optical properties of Cu-ZnO, Cu-CdO and CuO nanoparticles. Powder Technol. 214, 337–343. doi:10.1016/j.powtec.2011.08.025.

Williams, A.J., Grulke, C.M., Edwards, J., McEachran, A.D., Mansouri, K., Baker, N.C., Patlewicz, G., Shah, I., Wambaugh, J.F., Judson, R.S., Richard, A.M., 2017. The CompTox Chemistry Dashboard: a community data resource for environmental chemistry. J. Cheminform. 9. doi:10.1186/s13321-017-0247-6.

Singh, A.K., Bilal, M., Iqbal, H.M.N., Raj, A., 2021. Trends in predictive biodegradation for sustainable mitigation of environmental pollutants: recent progress and future outlook. Sci. Total Environ. 770. doi:10.1016/j.scitotenv.2020.144561.

Martin, T., Harten, P., Young, D., 2012. TEST (Toxicity Estimation Software Tool) Ver 4.1. U.S. Environ. Prot. Agency, Washington, DC EPA/600/C-12/006.

Joishy, S., Sindhu, H.S., Rajendra, B.V., 2018. Effect of cadmium dopant on structure and optical properties of ZnO thin films prepared by spray pyrolysis technique. IOP Conf. Ser. Mater. Sci. Eng. 360. doi:10.1088/1757-899X/360/1/012050.

Jiang, T., Wang, Y., Meng, D., Wang, D., 2016. One-step hydrothermal synthesis and enhanced photocatalytic performance of pine-needle-like Zn-doped CuO nanostructures. J. Mater. Sci. Mater. Electron. 27, 12884–12890. doi:10.1007/s10854-016-5424-2.

Yathisha, R.O., Nayaka, Y.A., Vidyasagar, C.C., 2016. Microwave combustion synthesis of hexagonal prism shaped ZnO nanoparticles and effect of Cr on structural, optical and electrical properties of ZnO nanoparticles. Mater. Chem. Phys. 181, 167–175. doi:10.1016/j.matchemphys.2016.06.046.

Vidyasagar, C.C., Hosamani, G., Kariyajjanavar, P., Yathisha, R.O., Arthoba Nayaka, Y., 2018. One-pot microwave synthesis and effect of Cu²⁺ ions on structural properties of Cu-ZnO NANO CRYSTals. Mater. Today Proc. 22171–22180. doi:10.1016/j.matpr.2018.06.582, Elsevier Ltd.

Chithambararaj, A., Sanjini, N.S., Bose, A.C., Velmathi, S., 2013. Flower-like hierarchical h-MoO3: new findings of efficient visible light driven nano photocatalyst for methylene blue degradation. Catal. Sci. Technol. 3, 1405–1414. doi:10.1039/c3cy20764a.

Vidyasagar, C.C., Naik, Y.A., Venkatesh, T.G., Viswanatha, R., 2011. Solid-state synthesis and effect of temperature on optical properties of Cu-ZnO, Cu-CdO and CuO nanoparticles. Powder Technol. 214, 337–343. doi:10.1016/j.powtec.2011.08.025.

Obeid, M.M., Jappor, H.R., Al-Marzoki, K., Al-Hydary, I.A., Edrees, S.J., Shukur, M.M., 2019. Unraveling the effect of Gd doping on the structural, optical, and magnetic properties of ZnO based diluted magnetic semiconductor nanorods. RSC Adv. 9, 33207–33221. doi:10.1039/c9ra04750f.

Mazhdi, M., Tafreshi, M.J., 2020. Gadolinium doping affecting on structural, magnetic and dielectric properties of ZnO nanoparticles. Appl. Phys. A Mater. Sci. Process. 126. doi:10.1007/s00339-020-3456-1.

Chandraboss, V.L., Karthikeyan, B., Senthilvelan, S., 2014. Experimental and first-principles study of guanine adsorption on ZnO clusters. Phys. Chem. Chem. Phys. 16, 23461–23475. doi:10.1039/c4cp03274h.

Aljawfi, R.N., Alam, M.J., Rahman, F., Ahmad, S., Shahee, A., Kumar, S., 2020. Impact of annealing on the structural and optical properties of ZnO nanoparticles and tracing the formation of clusters via DFT calculation. Arab. J. Chem. 13, 2207–2218. doi:10.1016/j.arabjc.2018.04.006.

Banu, K.B., Dheivamalar, S., 2020. l-Alanine adsorbed aluminum doped ZnO structures for nanocomposites with tailored photovoltaic properties: A DFT study. Funct. Compos. Struct. 2. doi:10.1088/2631-6331/abb51b.

Hadipour, N.L., Ahmadi Peyghan, A., Soleymanabadi, H., 2015. Theoretical study on the Al-doped ZnO nanoclusters for CO chemical sensors. J. Phys. Chem. C. 119, 6398–6404. doi:10.1021/jp513019z.

Li, D., Huang, J.F., Cao, L.Y., Ouyang, H.B., Li, J.Y., Yao, C.Y., 2014. Microwave hydrothermal synthesis of K+ doped ZnO nanoparticles with enhanced photocatalytic properties under visible-light. Mater. Lett. 118, 17–20. doi:10.1016/j.matlet.2013.12.052.

Raza, W., Faisal, S.M., Owais, M., Bahnemann, D., Muneer, M., 2016. Facile fabrication of highly efficient modified ZnO photocatalyst with enhanced photocatalytic, antibacterial and anticancer activity. RSC Adv 6, 78335–78350. doi:10.1039/c6ra06774c.

Adeel, M., Saeed, M., Khan, I., Muneer, M., Akram, N., 2021. Synthesis and characterization of Co-ZnO and evaluation of its photocatalytic activity for photodegradation of methyl orange. ACS Omega 6, 1426–1435. doi:10.1021/acsomega.0c05092.

Isai, K.A., Shrivastava, V.S., 2019. Photocatalytic degradation of methylene blue using ZnO and 2%Fe–ZnO semiconductor nanomaterials synthesized by sol–gel method: a comparative study. SN Appl. Sci. 1. doi:10.1007/s42452-019-1279-5.

Kenchappa Somashekharappa, K., Lokesh, S.V., 2021. Hydrothermal synthesis of K₂Ti₆O₁₃ nanotubes/nanoparticles: a photodegradation study on methylene blue and rhodamine B dyes. ACS Omega 6, 2857–2869. doi:10.1021/acsomega.0c02087.

Singh, M., Kumar, A., Krishnan, V., 2020. Influence of different bismuth oxyhalides on the photocatalytic activity of graphitic carbon nitride: a comparative study under natural sunlight. Mater. Adv. 1, 1262–1272. doi:10.1039/d0ma00294a.

Zheng, X., Yuan, J., Shen, J., Liang, J., Che, J., Tang, B., He, G., Chen, H., 2019. A carnation-like rGO/Bi₂O₂CO₃ /BiOCl composite: efficient photocatalyst for the degradation of ciprofloxacin. J. Mater. Sci. Mater. Electron. 30, 5986–5994. doi:10.1007/s10854-019-00898-w.

Mirzaeifard, Z., Shariatinia, Z., Jourshabani, M., Rezaei Darvishi, S.M., 2020. ZnO Photocatalyst revisited: effective photocatalytic degradation of emerging contaminants using S-doped ZnO nanoparticles under visible light radiation. Ind. Eng. Chem. Res. 59, 15894–15911. doi:10.1021/acs.iecr.0c03192.

Ghoderao, K.P., Jamble, S.N., Kale, R.B., 2019. Hydrothermally synthesized Cd-doped ZnO nanostructures with efficient sunlight-driven photocatalytic and antibacterial activity. J. Mater. Sci. Mater. Electron. 30, 11208–11219. doi:10.1007/s10854-019-01466-y.

Phuruangrat, A., Mad-Ahin, S., Yayapao, O., Thongtem, S., Thongtem, T., 2015. Photocatalytic degradation of organic dyes by UV light, catalyzed by nanostructured Cd-doped ZnO synthesized by a sonochemical method. Res. Chem. Intermed. 41, 9757–9772. doi:10.1007/s11164-015-1963-z.

Zhang, D., Zeng, F., 2012. Visible light-activated cadmium-doped ZnO nanostructured photocatalyst for the treatment of methylene blue dye. J. Mater. Sci. 47, 2155–2161. doi:10.1007/s10853-011-6016-4.

Khayyat, S.A., Abaker, M., Umar, A., Alkattan, M.O., Alharbi, N.D., Baskoutas, S., 2012. Synthesis and characterizations of Cd-doped ZnO multipods for environmental remediation application. J. Nanosci. Nanotechnol. 12, 8453–8458. doi:10.1166/jnn.2012.6801.

Zhai, Y.J., Li, J.H., Fang, X., Chen, X.Y., Fang, F., Chu, X.Y., Wei, Z.P., Wang, X.H., 2014. Preparation of cadmium-doped zinc oxide nanoflowers with enhanced photocatalytic activity. Mater. Sci. Semicond. Process. 26, 225–230. doi:10.1016/j.mssp.2014.04.023.

Dumrongrojthanath, P., Phuruangrat, A., Thongtem, S., Thongtem, T., 2021. Photocatalysis of Cd-doped ZnO synthesized with precipitation method. Rare Met. 40, 537–546. doi:10.1007/s12598-019-01283-6.

He, H., Yang, S., Yu, K., Ju, Y., Sun, C., Wang, L., 2010. Microwave induced catalytic degradation of crystal violet in nano-nickel dioxide suspensions. J. Hazard. Mater. 173, 393–400. doi:10.1016/j.jhazmat.2009.08.084.

Abbas, H.A., Nasr, R.A., Abu-Zurayk, R., Al Bawab, A., Jamil, T.S., 2020. Decolourization of crystal violet using nano-sized novel fluorite structure Ga₂Zr₂₋ₓWₓO₇ photocatalyst under visible light irradiation. R. Soc. Open Sci. 7. doi:10.1098/rsos.191632.

Jayaraman, V., Ayappan, C., Palanivel, B., Mani, A., 2020. Bridging and synergistic effect of the pyrochlore like Bi₂Zr₂O₇ structure with robust CdCuS solid solution for durable photocatalytic removal of the organic pollutants. RSC Adv. 10, 8880–8894. doi:10.1039/d0ra00644k.

Djellabi, R., Ghorab, M.F., Cerrato, G., Morandi, S., Gatto, S., Oldani, V., Di Michele, A., Bianchi, C.L., 2015. Photoactive TiO₂-montmorillonite composite for degradation of organic dyes in water. J. Photochem. Photobiol. A Chem. 295, 57–63. doi:10.1016/j.jphotochem.2014.08.017.

Rao Akshatha, S., Sreenivasa, S., Parashuram, L., Raghu, M.S., Yogesh Kumar, K., Madhu Chakrapani Rao, T., 2020. Visible-light-induced photochemical hydrogen evolution and degradation of crystal violet dye by interwoven layered MoS₂/Wurtzite ZnS Heterostructure Photocatalyst. ChemistrySelect 5, 6918–6926. doi:10.1002/slct.202001914.

Li, W., Liu, Z., Song, W., Xu, Y., 2020. Ag2S quantum-dot-modified flower-like PbBiO₂Br for enhanced photocatalytic degradation of crystal violet. J. Mater. Sci. Mater. Electron. 31, 18495–18506. doi:10.1007/s10854-020-04393-5.

Lin, H.P., Chen, C.C., Lee, W.W., Lai, Y.Y., Chen, J.Y., Chen, Y.Q., Fu, J.Y., 2016. Synthesis of a SrFeO3-x/g-C3N4 heterojunction with improved visible-light photocatalytic activities in chloramphenicol and crystal violet degradation. RSC Adv. 6, 2323–2336. doi:10.1039/c5ra21339h.

Ma, F., Yang, Q., Wang, Z., Liu, Y., Xin, J., Zhang, J., Hao, Y., Li, L., 2018. Enhanced visible-light photocatalytic activity and photostability of Ag₃PO₄/Bi₂WO₆ heterostructures toward organic pollutant degradation and plasmonic Z-scheme mechanism. RSC Adv. 8, 15853–15862. doi:10.1039/c8ra01477a.

Cherrak, R., Hadjel, M., Benderdouche, N., Adjdir, M., Mokhtar, A., Khaldi, K., Sghier, A., Weidler, P.G., 2020. Preparation of nano-TiO₂/diatomite composites by non-hydrolytic sol–gel process and its application in photocatalytic degradation of crystal violet. Silicon 12, 927–935. doi:10.1007/s12633-019-00186-6.

Bargozideh, S., Tasviri, M., 2018. Construction of a novel BiSI/MoS₂ nanocomposite with enhanced visible-light driven photocatalytic performance. New J. Chem. 42, 18236–18241. doi:10.1039/c8nj04102d.

Vinosel, V.M., Anand, S., Janifer, M.A., Pauline, S., Dhanavel, S., Praveena, P., Stephen, A., 2019. Enhanced photocatalytic activity of Fe₃O₄/SnO₂ magnetic nanocomposite for the degradation of organic dye. J. Mater. Sci. Mater. Electron. 30, 9663–9677. doi:10.1007/s10854-019-01300-5.

M.F. Sanakousar, Vidyasagar. C.C, Victor M. Jiménez-Pérez et al.

Journal of Hazardous Materials Advances 2 (2021) 100004

Sharma, M., Jain, T., Singh, S., Pandey, O.P., 2012. Photocatalytic degradation of organic dyes under UV-Visible light using capped ZnS nanoparticles. Sol. Energy 86, 626–633. doi:10.1016/j.solener.2011.11.006.

Mittal, M., Sharma, M., Pandey, O.P., 2014. Photocatalytic studies of crystal violet dye using Mn doped and PVP capped ZnO nanoparticles. J. Nanosci. Nanotechnol. 14, 2725–2733. doi:10.1166/jnn.2014.8615.

Mohamed, S.K., Hegazy, S.H., Abdelwahab, N.A., Ramadan, A.M., 2018. Coupled adsorption-photocatalytic degradation of crystal violet under sunlight using chemically synthesized grafted sodium alginate/ZnO/graphene oxide composite. Int. J. Biol. Macromol. 108, 1185–1198. doi:10.1016/j.ijbiomac.2017.11.028.

Dargahi, M., Masteri-Farahani, M., Shahsavarifar, S., Feizi, M., 2020. Microemulsion-mediated preparation of $Ce_2(MoO_4)_3$ nanoparticles for photocatalytic degradation of crystal violet in aqueous solution. Environ. Sci. Pollut. Res. 27, 12047–12054. doi:10.1007/s11356-020-07816-2.

Ahmad, W., Khan, A., Ali, N., Khan, S., Uddin, S., Malik, S., Ali, N., Khan, H., Khan, H., Bilal, M., 2021. Photocatalytic degradation of crystal violet dye under sunlight by chitosan-encapsulated ternary metal selenide microspheres. Environ. Sci. Pollut. Res. 28, 8074–8087. doi:10.1007/s11356-020-10898-7.

Kossar, S., Banu, I.B.S., Aman, N., Amiruddin, R., 2020. Investigation on photocatalytic degradation of crystal violet dye using bismuth ferrite nanoparticles. J. Dispers. Sci. Technol. 0, 1–10. doi:10.1080/01932691.2020.1806861.

Rahmat, M., Rehman, A., Rahmat, S., Bhatti, H.N., Iqbal, M., Khan, W.S., Bajwa, S.Z., Rahmat, R., Nazir, A., 2019. Highly efficient removal of crystal violet dye from water by MnO_2 based nanofibrous mesh/photocatalytic process. J. Mater. Res. Technol. 8, 5149–5159. doi:10.1016/j.jmrt.2019.08.038.

Abdi, M., Balagabri, M., Karimi, H., Hossini, H., Rastegar, S.O., 2020. Degradation of crystal violet (CV) from aqueous solutions using ozone, peroxone, electroper-oxone, and electrolysis processes: a comparison study. Appl. Water Sci. 10, 1–10. doi:10.1007/s13201-020-01252-w.

Ameen, S., Akhtar, M.S., Nazim, M., Shin, H.S., 2013. Rapid photocatalytic degradation of crystal violet dye over ZnO flower nanomaterials. Mater. Lett. 96, 228–232. doi:10.1016/j.matlet.2013.01.034.

Grulke, C.M., Williams, A.J., Thillanadarajah, I., Richard, A.M., 2019. EPA's DSSTox database: history of development of a curated chemistry resource supporting computational toxicology research. Comput. Toxicol. 12. doi:10.1016/j.comtox.2019.100096.

Ferri, P., Ramil, M., Rodríguez, I., Bergamasco, R., Vieira, A.M.S., Cela, R., 2017. Assessment of quinoxyfen phototransformation pathways by liquid chromatography coupled to accurate mass spectrometry. Anal. Bioanal. Chem 409, 2981–2991. doi:10.1007/s00216-017-0241-x.